UNIVERSITY OF NORTH CAROLINA CHAPEL HILL

Construction and Characterization of an NMR Spectrometer Operating at Earth's Magnetic Field

by

Boris Mesits

A thesis submitted in partial fulfillment for the requirements of the Honors distinction.

under the direction of

Rosa Tamara Branca

Department of Physics and Astronomy

May 2020

Declaration of Authorship

I, BORIS MESITS, declare that this thesis titled, "Construction and Characterization of an NMR Spectrometer Operating at Earth's Magnetic Field" and the work presented in it are my own. I confirm that:

- This work was done wholly or mainly while in candidature for a degree at this University.
- Where any part of this thesis has previously been submitted for a degree or any other qualification at this University or any other institution, this has been clearly stated.
- Where I have consulted the published work of others, this is always clearly attributed.
- I have acknowledged all main sources of help.
- Where the thesis is based on work done by myself jointly with others, I have made clear exactly what was done by others and what I have contributed myself.

Signed: _____

Date: _____

UNIVERSITY OF NORTH CAROLINA CHAPEL HILL

Abstract

Advisor: Rosa Tamara Branca
Department of Physics and Astronomy

Bachelor of Science

by Boris Mesits

Spin is a property of many nuclei which can be exploited for imaging and spectroscopy with nuclear magnetic resonance (NMR) studies. While most medical applications of NMR require large magnets to create the resonance phenomenon, the natural magnetic field of the Earth can also serve the same purpose. Although spectral resolution is lower due to the relatively weak field of the Earth, the continuous presence of this natural field provides an opportunity for easy application of NMR techniques in the field.

To access this opportunity, we build and characterize the performance of a low-cost, portable NMR spectrometer, based on the design published by Michal (2010). A standard microcontroller, fed with open-source pulse programming software from a typical laptop, operates the experiment's coil, removing the need for an expensive proprietary controller. We find that the system, despite its simplicity, is susceptible to unwanted feedback-driven oscillations in the output signal, which depends sensitively on the layout of the electronic components. We show that these oscillations may be due both to inductive coupling of ground wires to amplifier outputs, and to signal-ground coupling inherent to the microcontroller. After removing the feedback-driven oscillations, we demonstrate one potential use of the spectrometer as a one-dimensional imager.

Acknowledgements

Some text and figures that appear here were previously submitted as coursework for PHYS395 and PHYS691H. We note that the breadboard circuit, mentioned in the conclusion, was built by Nick Bryden.

I would like to thank Rosa Tamara Branca for the rewarding opportunity to focus on undergraduate research for two years. I must also thank Michael Antonacci, Nick Bryden, and Michele Kelly for their steady guidance during our shared time in the laboratory. I owe further gratitude to Rose Vigil for her support and logistical assistance. Finally I give my thanks to George Edwards, a valued colleague and a tremendous reservoir of wires and patience.

Contents

Declaration of Authorship i

Abstract ii

Acknowledgements iii

Abbreviations vi

1 Background 1
- 1.1 Nuclear Magnetic Resonance . . . 1
- 1.2 Free Induction Decay . . . 3
- 1.3 Earth's Field NMR . . . 6
- 1.4 Applications . . . 7
- 1.5 Objective . . . 7

2 Circuit Design 8
- 2.1 General Approach . . . 8
- 2.2 Microcontroller . . . 10
- 2.3 Transmitter . . . 11
- 2.4 Receiver . . . 12

3 Development and Experiment 13
- 3.1 In-Lab Board Manufacturing . . . 13
- 3.2 Professionally-Printed Board . . . 17
- 3.3 Calibration of Bc Frequency and Duration . . . 17
- 3.4 Shimming of Earth's Field and Gradient Coil Tests . . . 18
- 3.5 Change in Inductance from Shielding . . . 19
- 3.6 Pre-Polarization of Nuclear Spins . . . 19
- 3.7 Compatibility of Arduino Uno and Arduino Mega . . . 20
- 3.8 Outdoor Experiments . . . 21
- 3.9 Active Shimming . . . 21
- 3.10 Linewidth . . . 22
- 3.11 Variation of Bc Duration . . . 24

4 Hardware Performance **26**
4.1 Hysteresis . . . 26
4.2 Effect of PCB Design on Feedback Oscillations . . . 28
4.3 Effect of Ground Wire Placement . . . 28
4.4 Effect of Analog Input Connections on Feedback Oscillations . . . 29
4.5 Test with Unity-Gain Amplifier on Analog Input . . . 29
4.6 Test with Second Microcontroller . . . 30
4.7 Initiation Timing of Feedback Oscillations . . . 30
4.8 Other Observations . . . 30

5 Parasitic Inductance Analysis **32**
5.1 Theoretical Framework . . . 32
5.2 Numerical Implementation . . . 34
5.3 Results . . . 37

6 Conclusions **38**
6.1 Feedback Oscillations . . . 38
6.2 PCB Development . . . 38
6.3 Experimental Parameters . . . 39
6.4 Note on Unusual Circumstances . . . 39
6.5 Summary . . . 40

A Validation of Induction Model **41**

Bibliography **44**

Abbreviations

NMR	Nuclear Magnetic Resonance
EFNMR	Earth Field NMR
PCB	Printed Circuit Board
FID	Free Induction Decay
T/R	Transmit/Receive
EM	Electromagnetic
AC	Alternating Current
DC	Direct Current
FWHM	Full-Width Half Maximum
EMF	Electromotive Force
MRI	Magnetic Resonance Imaging
SNR	Signal-to-Noise Ratio

Dedicated to my mother and father

Chapter 1

Background

1.1 Nuclear Magnetic Resonance

Nuclear magnetic resonance (NMR) is a physical phenomenon that enables some of the most sophisticated imaging and chemical detection techniques today. [1] [2] Rapid advances in medicine followed the advent of magnetic resonance imagining (MRI), an application of NMR physics. The non-invasive nature of NMR is of key importance to *in vivo* biological studies. [3] Chemists use NMR spectroscopy to determine the composition of complex mixtures, and to monitor the progress of chemical reactions. [2]The structure of molecules may be deduced from NMR spectroscopy as well, as in the famous example of buckminsterfullerenes. [1]

The phenomenon of NMR was first discovered in 1946 due to experiments by Felix Bloch and Edward Mills Purcell. [1] They detected the NMR phenomenon of spins placed in a strong magnetic field by directly detecting the current induced on a coil by the precession of water spins in a strong magnetic field. [6] Nuclei such as protons (the Hydrogen ion) or ^{31}P have a permanent magnetic dipole moment. This is due to the intrinsic spin of the nucleons, protons and neutrons, each having spin 1/2. Inside a nucleus, the spins of the protons and neutrons group in opposite-spin pairs, canceling out the net magnetic dipole. However, for nuclei with an odd numbers of protons, an odd number of neutrons, or both, the spins cannot fully cancel out, and the nucleus maintains a dipole moment. [4]

Quantum mechanically, when a spin 1/2 particle (as is the case for protons in water, the subject of this work) is placed in a magnetic field, its S_z component can assume either the value of $+1/2\hbar$ or the value $-1/2\hbar$.

For a large collection of nuclear spins (such as one in a macroscopic sample), there will be a distribution of spins with their S_z component equal to $+1/2\hbar$ ($N^{\uparrow}$, or parallel configuration) and with their S_z component equal to -1/2$\hbar$ ($N^{\downarrow}$, antiparallel configuration). The ratio between $N^{\uparrow}$ and $N^{\downarrow}$ is given by: [4]

$$\frac{N^{\uparrow}}{N^{\downarrow}} = \exp\left(\frac{-\mu B_0}{kT}\right) \tag{1.1}$$

where μ is the magnetic dipole moment associated with the nuclear spin, B_0 is the magnitude of the magnetic field $\mathbf{B}_0$, and T is the temperature. [4] [5] For typical experimental values of T and B_0, the ratio $N^{\uparrow}/N^{\downarrow}$ is very close to one, with only a slight excess of spins in the $S_z = +1/2\hbar$ configuration. The excess of spins in the $+1/2\hbar$ configuration will give rise to the magnetization $\mathbf{M}$, described by

$$\mathbf{M} \propto \left(N^{\uparrow} - N^{\downarrow}\right)\hat{\mathbf{k}} \tag{1.2}$$

a vector that points along the z-direction. In NMR and MRI experiments one detects the magnetization, (not the single spins) whose dynamic evolution under the effect of radio frequency pulses can be described classically. [5] The magnetization $\mathbf{M}$, when perturbed from equilibrium in the presence of the magnetic field $\mathbf{B}_0$, rotates about the z-axis at a frequency ω_L (gyroscopic precession of the magnetization). This frequency, called the Larmor frequency, is proportional to the strength of the magnetic field B_0

$$\omega_L = B_0\gamma \tag{1.3}$$

giving rise to the proportionality constant γ called the *gyromagnetic ratio*, characteristic to the specific nucleus.

In order to perturb the magnetization from equilibrium, a second magnetic field orthogonal to $\mathbf{B}_0$, with a frequency equal to the Larmor frequency, is typically applied. Specifically, if the magnetization is at its equilibrium, oriented along the z-axis, and a second oscillating magnetic field is applied orthogonal to the z-direction at a frequency equal to the *Larmor frequency* (resonance condition), the magnetization $\mathbf{M}$ starts to precess around the transverse field and can be effectively rotated away from the z-axis. The angle of rotation around the transverse magnetic field is proportional to the strength and duration of the transverse magnetic field.

The most direct application of the nuclear magnetic resonant phenomenon has been for NMR spectroscopy. In this technique, the external magnetic field $\mathbf{B}_0$ polarizes the nuclear spins of some nuclei in a chemical or biological sample. Once the magnetization is rotated away from the z-axis, under the effect of $\mathbf{B}_0$ it will continue to precess. The precession of the magnetization around the z-axis can create a current in a coil placed

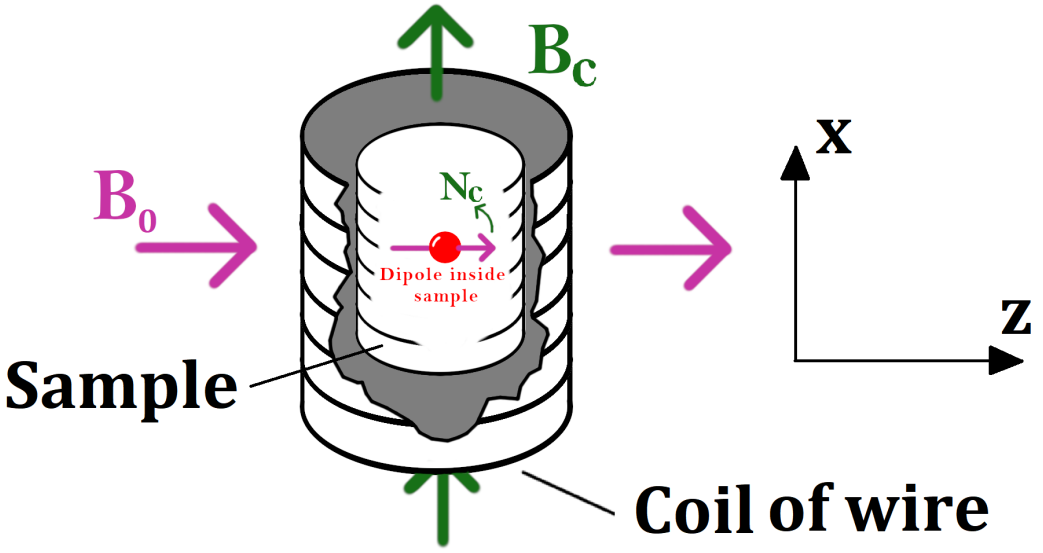

FIGURE 1.1: Simplified schematic of basic NMR spectroscopy.

orthogonal to the z-axis. This current is the NMR signal. By taking the Fourier transform of the signal, one can measure the magnetization precession frequency, which is characteristic of the atom and the molecule in which the atom resides. (see Figure 1.1). The Fourier transform of the NMR signal, called the NMR spectrum, can have one or more peaks. A peak at frequency ω indicates that a species of nucleus with gyromagnetic ratio ω/B_0 is present in the sample. Measuring the applied magnetic field yields the gyromagnetic ratio for each peak. Since each species of nucleus has a known ratio, the composition of the sample may be deduced (see Figure 1.2).

The shape, duration, and number of magnetic pulses applied to the sample is a broad topic with many applications. [4] [1] Here narrow our attention to a simple type of NMR spectroscopy, the Free Induction Decay experiment.

1.2 Free Induction Decay

When the transverse magnetic field is turned off, the magnetization continues to precess around the z-axis, under the effect of the magnetic field $\mathbf{B}_0$, at the Larmor frequency. The precession does not last forever but it will decay with a time constant called the transverse relaxation time T_2. [4] The detected decaying signal is called Free Induction Decay (FID).

A primary consideration of an NMR experiment is to excite the spins of the nuclei so as to generate the maximum signal response. The signal is strongest when $\mathbf{B}_c$ oscillates

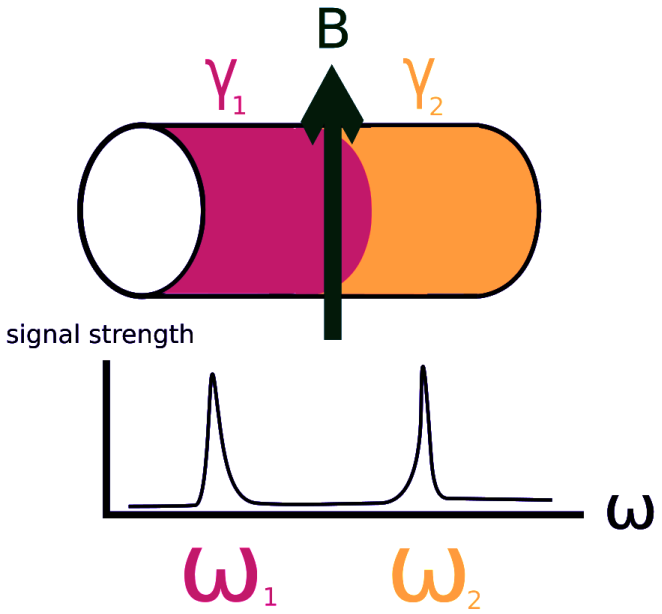

FIGURE 1.2: A visualization of basic NMR spectroscopy. If the differently colored regions represent regions of nuclei with different gyromagnetic ratios, then the two materials may be distinguished in the Fourier spectrum via Equation 1.1.

at the resonant frequency ω_L. The signal strength also depends on the magnetization angle θ, which is increased by increasing the magnitude and duration of the additional field $\mathbf{B}_c$. The maximum signal is achieved when $\theta = \pi/2$, when the magnetization is entirely within the x-y plane, orthogonal to $\mathbf{B}_0$. As a result, it is possible to *over*-excite the spins by pulsing for too long or by using a too strong magnetic field $\mathbf{B}_c$. For dipoles in this state, any further excitation will extend the angle beyond $\theta = \pi/2$ and the signal will begin to diminish.

The duration of data collection is also an important consideration in NMR. Collecting more data increases the resolution of the signal in the frequency domain at the expense of increasing spectrum noise. As a result, it is best to stop collecting data when the the signal reaches noise level. Any additional data collected will add more noise than signal to the Fourier spectrum.

At the same time, longer data collection times result in higher resolution in the spectral domain, according to the Nyquist theorem, [7] making longer collection times desirable when possible. As a result, reduction in the signal-to-noise ratio (SNR) allows for higher resolution data. A higher resolution means that closely-spaced peaks can be easily distinguished, leading to more precise spectroscopic measurements and better discrimination of nuclear species. However, even a high-resolution spectrum may be muddled by large linewidths. If the individual peaks are spread out over a range of frequencies, the

boundaries between the two may overlap and the distinction may disappear. Furthermore, wide peaks are typically associated with low SNR. Small linewidths are especially important for a more sophisticated measurement achievable through free-induction decay - a one-dimensional spin density image.

While NMR spectroscopy can distinguish between different species of nuclei, it can also be used to spatially locate the spins, when used in conjunction with a magnetic field gradient. In the former case, the observed frequencies may vary because of different gyromagnetic ratios or chemical composition of the sample. In the latter case, however, frequencies vary because of an inhomogeneous magnetic field $\mathbf{B}_0$. By applying a different magnetic field to different regions of a sample, the frequencies of precession will correspondingly vary, assigning a frequency to each location along the magnetic field gradient (see Figure 1.3). By applying a magnetic field gradient applied along the x-direction, for example, will spatially label the spin along that direction. In the frequency domain, the signal will be nothing else than the projection of the sample spin density along the direction of the applied gradient. In the one-dimensional case, the extraction of an image is remarkably simple.

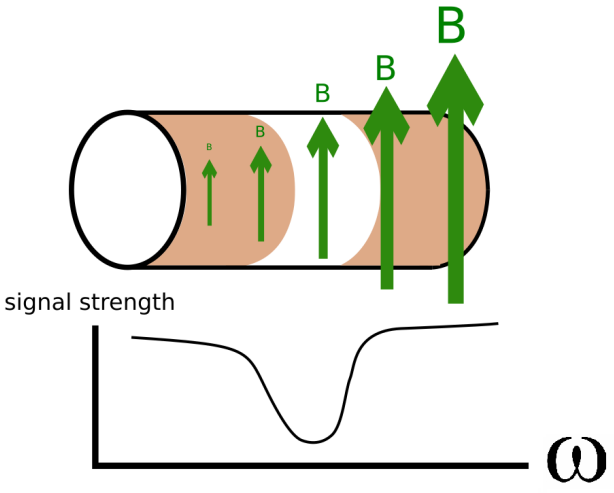

FIGURE 1.3: A visualization of one-dimensional imaging with NMR. If the colored region represents the presence of a substance with resonant nuclei, then the empty region in the center will not produce a signal. The variable magnetic field will then generate a gap in the spectrum at the corresponding Larmor frequency.

The strength of the signal is proportional to the concentration of nuclei in the sample. Regions of the sample with fewer precessing nuclei will generate a weaker signal, resulting in a dip in the spectrum. Similarly, an excess of precessing nuclei creates a peak in the spectrum. In other words, the shape of the signal in frequency space is a reflection of the sample spin density along the direction of the magnetic field gradient. If the frequency spread generated by the magnetic field gradient is smaller than the frequency spread

characteristic of the nuclei in different molecules, then the technique becomes a way to spatially resolve the chemical composition of a sample.

The manifestations of NMR techniques take many forms. The next section introduces a subset of NMR experiments that is the topic of this dissertation.

1.3 Earth's Field NMR

Nuclear magnetic resonance spectroscopy is typically performed by using strong electromagnets which make the resulting signal easier to detect. For magnetic fields on the order of Tesla, the Larmor frequency is in the radio frequency range. These equipments are expensive and motivated the search for cheaper alternatives. The Earth naturally provides a magnetic field which is only about 50 μT but can be used in the place of artificial magnetic fields. The ubiquity and uniformity of this field makes Earth field nuclear magnetic resonance (EFNMR) a suitable solution for low-field spectroscopy.

Environmental study is an important motivation for EFNMR spectroscopy. [8]. Because the equipment involved lacks large electromagnets, the electronics can be powered by portable batteries. Portability is a major advantage of the design. Furthermore, while the Earth's magnetic field is weak, resulting in smaller magnetization (see Equation 1.1), the field is generally quite homogeneous. The importance of this homogeneity stems from the fact that dipole precession occurs everywhere in the sample, and the full volume of the sample contributes to the FID signal. If the Earth's field is inhomogeneous throughout the sample, the Larmor frequency also would be non-uniform, causing a frequency spread in the spectral domain. Because the Earth's field is very homogeneous, a very narrow peak can be generated.

One way to overcome the inherently weaker FID signal in EFNMR is by pre-polarizing the sample prior to the measurement. When a sample is removed from a magnetic field, its magnetization does not immediately disappear. Instead, the excess of aligned dipoles $N^{\uparrow} - N_{\downarrow}$ decays with a time constant T_1, the longitudinal relaxation time. [4]. The magnetization vector will align with any external field, whether the external field generated the magnetization or not. To augment the magnetization of a sample while still using Earth's field, the sample can be placed in a strong magnetic field, where it acquires a larger magnetization. Then the sample is rapidly placed in the more homogeneous Earth's magnetic field before the magnetization returns to thermal equilibrium value. Using this method, the advantages of a strong signal and homogeneous field are combined.

1.4 Applications

The advantages of portable EFNMR are ideal for certain environmental research applications because *in situ* analysis is often a great asset. An example application was provided by Callaghan et al. in Antarctic sea ice. [8]. EFNMR spectroscopy was used to investigate the structure and distribution of brine pockets in sea ice, to better understand the ice's physical properties for use in climate modeling. Ice cores were collected on-site, but transport to a lab away was not possible because the changing temperatures and humidities during transport would damage the samples. The harsh conditions of the site made traditional NMR impractical. Instead, an EFNMR spectrometer, similar to the design presented here, was used to test samples soon after extraction. In their 1990 article, Stepisnik et. al. cite the lower cost of EFNMR as motivation for their two-dimensional imager. [9]

1.5 Objective

This dissertation aims to realize a low-cost EFNMR spectrometer based on a design provided by Michal [10]. Michal's work attempted to provide a means for small labs, students, and amateurs to access NMR spectroscopy. In this work, we investigate the advantages and possible pitfalls of the design by conducting free-induction decay experiments on water samples. We also evaluate the potential of the design as a platform for one-dimensional imaging, using a gradient coil to generate the inhomogeneous magnetic field.

Chapter 2

Circuit Design

2.1 General Approach

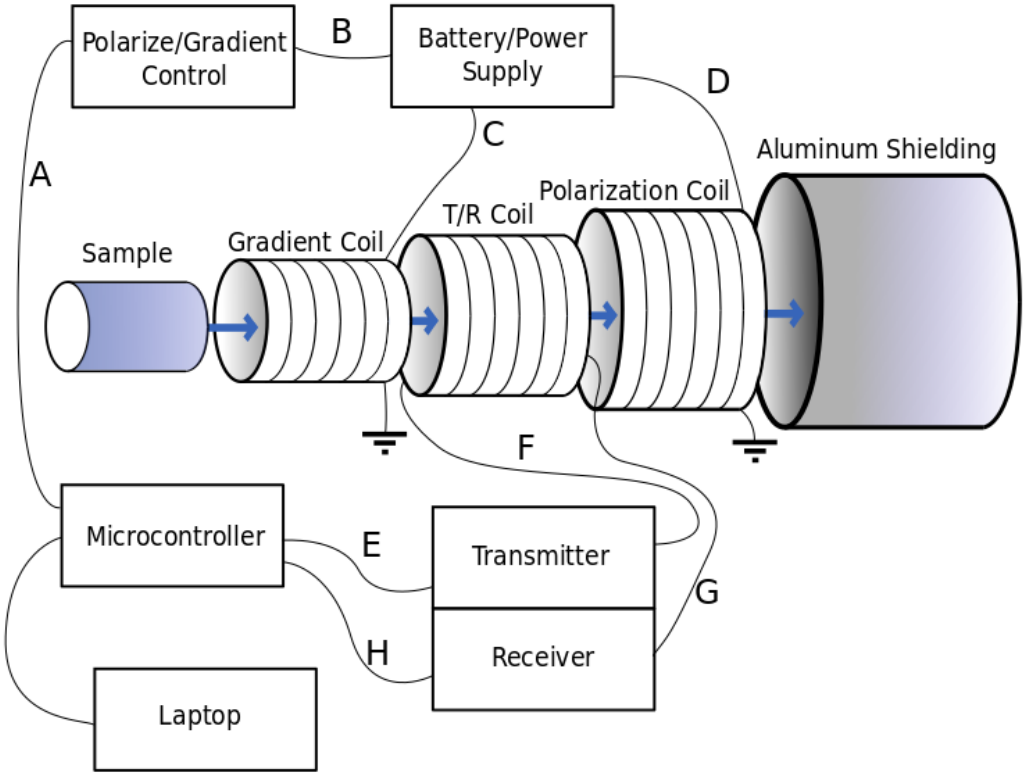

FIGURE 2.1: Schematic layout of experiment.

The purpose of the EFNMR spectrometer is to measure free-induction decay signals from precessing magnetic dipoles in a sample and extract their Larmor frequency. Therefore, a coil is needed to induce an oscillating magnetic field in the sample. In addition, a

coil is needed around the sample to detect the dipole precession. In fact, the same coil can accomplish both tasks. A laptop computer powers a microcontroller and uploads the programs to control the experiment (see Figure 2.1). The microcontroller actives a power supply control circuit (**A**) which supplies current to the polarization coil (**B**) and gradient coil (**C**). After a time larger than T_1, the polarization coil is turned off adiabatically to allow the sample's magnetization to align along the Earth's magnetic field. Then the microcontroller initiates the oscillating field $\mathbf{B}_c$ (**D**), generated with the transmitter, which enters the T/R coil (**F**), rotating the nuclear spin magnetization by an angle θ. The free precession of the transverse magnetization around the Earth magnetic field induces a voltage in the T/R coil. The receiver opens and detects the signal (**G**) before relaying the data to the microcontroller (**H**).

The oscillating magnetic field $\mathbf{B}_c$ is generated by passing an oscillating current at the desired frequency through the coil. This oscillating current is supplied with the transmitter, which ensures the magnetic perturbation successfully causes dipole precession. The receiver amplification is necessary to boost the detected signal to a strength that the microcontroller's ADC (analog-digital converter) can detect. These considerations and those of filtering are discussed in the **Receiver** section.

The key components of the EFNMR spectrometer are:

- transmit/receive (T/R) coil - needed to induce an oscillating magnetic field $\mathbf{B}_c$ transverse to the main magnetic field $\mathbf{B}_0$, and to detect the precession of the transverse magnetization around the main magnetic field $\mathbf{B}_0$
- transmitter - made up of a microcontroller and an amplifying/filtering circuit, needed to supply the $\mathbf{B}_c$ field
- receiver - uses the microcontroller and a separate amplification/filtering circuit, needed for receiving and filtering of the dipole precession signal from coil
- microcontroller - Arduino Uno or Mega programmed with open-source software, available at *http://www.phas.ubc.ca/~michal/Earthsfield*, controls operation of experiment
- sample - water bottle placed into T/R coil
- laptop - used to store the collected data and interfaces with the microcontroller via USB cable
- gradient coil - two narrow loops of wire that carry enough current to create a relatively linear magnetic field inhomogeneity

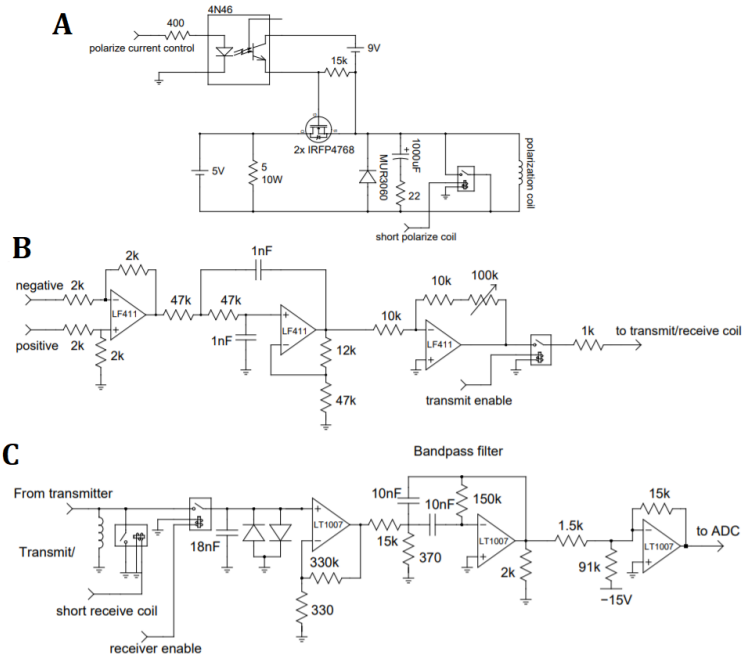

FIGURE 2.2: Schematics for the transmitter, receiver, and polarization control circuit. Adapted from Michal [10].

- polarization coil - large coil placed on the outside of the T/R coil to generate a large, temporary magnetic field that polarizes the spins

Not shown in Figure 2.1 is the magnetic probe, used to measure B_0 for calculating ω_L. Most modern cell phones contain a probe that indicates the strength and direction of magnetic fields with reasonable accuracy.

We base our design for the circuit on the design provided by Michal [10]. The schematics of the transmitter, receiver, and polarization control circuit are shown in Figure 2.2. The gradient control circuit, not provided by Michal, is very simple. It consists of a reed relay that connects a battery to the gradient coil when activated by the microcontroller (see 3.5).

2.2 Microcontroller

For our simple FID experiment - i.e. excitation of the magnetization and acquisition of the FID - the software configures the Arduino to output two digital waveforms at the necessary frequency, phase, and duty cycle for the transmitter to combine them into a zero-centered sinusoidal pulse. The software programs digital signals to be sent to relays on the circuit board (see Figure 2.3). The built in analog-digital converter on

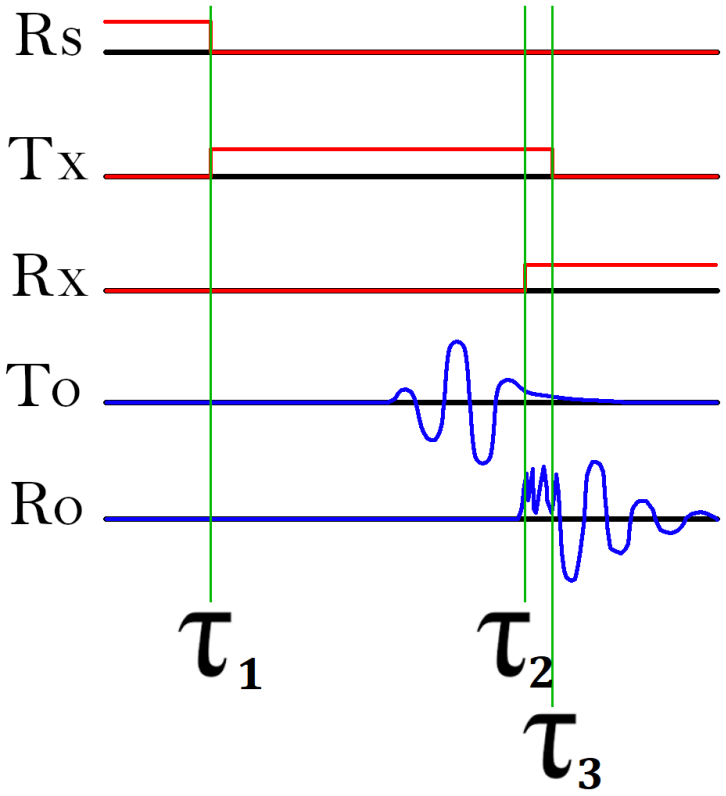

FIGURE 2.3: Timing diagram for the communication between the microcontroller and T/R circuit. First, at about τ_1, the receive short (Rs) signal deactivates, which disconnects the coil from ground (which otherwise prevents the coil from acquiring a floating voltage). Simultaneously, the transmit connect (Tx) signal connects the transmitter to the coil. At some later time, the signal is transmitted, as seen in the transmitter output (To). When the receiver is activated by the receiver connect (Rx), a signal passes through the output of the receiver (Ro). The duration of the signal is controlled by the microcontroller's software. The difference between τ_1 and τ_2 is about 60 ms, whereas between τ_2 and τ_3 only about 2 ms elapse.

the Arduino is used to capture data from the output of the receiver. The software then allows the data to be visualized and stored.

2.3 Transmitter

The transmitter must convert a digital (pulse-width modulated) waveform from the microcontroller to a sinusoidal waveform of a short duration with no DC offset. To achieve the resonant condition, and effectively rotate the magnetization onto the transverse plane, the frequency of this waveform must be equal to ω_L. The microcontroller outputs a typical digital voltage of 0 or 5V. To create a zero-centered pulse, we follow the design provided by Michal. First two digital signals, exactly out of phase, with duty cycle of about 0.4, are passed into a summing amplifier, with one of the signals connected to the inverting input.

After this stage, the transmitted signal is smoothed into a sinusoid with a low-pass filter. A final stage carries out further amplification, with adjustable gain provided by adding a potentiometer as a feedback resistor. We label the final voltage amplitude of the transmitted waveform V_T. Varying the strength of the transmitter output changes the strength of the field $\mathbf{B}_c$ and the angle of rotation of the magnetization away from the z-axis. Increasing the V_T has a similar effect to increasing the $\mathbf{B}_c$ duration.

2.4 Receiver

The receiver carries the task of amplifying the tiny NMR signal from the T/R coil. Amplification is necessary to bring the strength of the signal within the dynamic range of the analog-digial converter (ADC). It also performs a bandpass filtering stage to process the signal before conversion into digital data by the microcontroller. The last stage of the receiver performs some amplification, but more importantly it includes a "pull-up" resistor that increases the center voltage of the signal from zero to about 2.5 volts. This is necessary because the microcontroller has an ADC that only reads from zero to 5 volts. In other words, the "bottom half" of the signal would be lost without this final stage.

The bandpass filter must be tuned to the signal frequency ω_L. For protons in water, the gyromagnetic ratio is 42.6 MHz/Tesla, corresponding to 2130 Hz for a typical Earth field strength (50 μT). The receiver places the T/R coil in series with an inductor to create a resonant LCR circuit that amplifies signals within a given frequency range. The resonant frequency in terms of the T/R coil inductance L and the capacitor value C is

$$\omega_0 = \frac{1}{\sqrt{LC}} \tag{2.1}$$

To maximize signal strength, the LCR circuit frequency ω_0 must also equal ω_L.

Chapter 3

Development and Experiment

Although the schematic design from Michal [10] details the theoretical function of the electronics, a practical spectrometer requires careful consideration regarding the placement and maintenance of components. In this chapter, we outline the prototyping process that led to a functional spectrometer and demonstrate how experiments were conducted.

3.1 In-Lab Board Manufacturing

The costs and wait time associated with ordering printed circuit boards from a manufacturer prompted an attempt to print a prototype board in the lab.

A circuit design was drawn using the ExpressPCB software and the photo editor GIMP. This black-and-white photo (see Figure 3.1) was printed onto magazine paper. The ink was transferred to a copper-coated silicon board by pressing the paper onto the copper with a hot iron after soaking the paper in water. Then the ink-imprinted boards were placed into a ferric acid solution for 10 to 20 minutes, until all the exposed, ink-free copper dissolved away, leaving only the printed design. The result is a functional printed circuit board, as shown in Figure 3.2.

Important notes from the printing process include:

- Large pads for solder joints are essential since all of the parts must be surface-mounted.
- The ink from the magazine paper does not always cleanly adhere to the copper surface - it is often necessary to fill in missing sections of ink with a permanent marker.

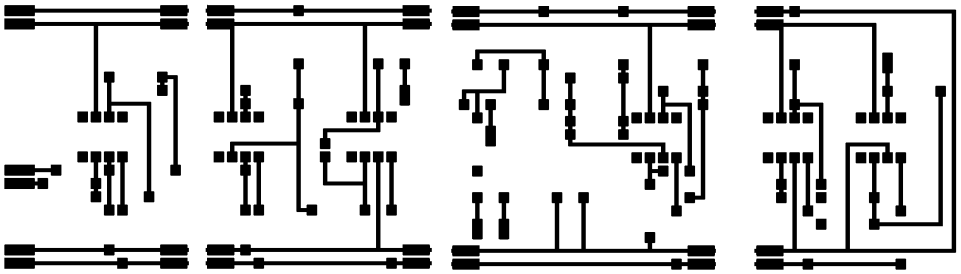

FIGURE 3.1: The design for the lab-manufactured board. Note the four separate segments, which allow the design to printed on smaller silicon pieces.

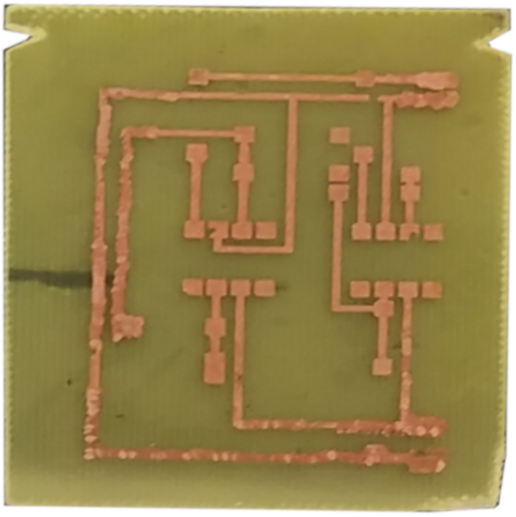

FIGURE 3.2: A segment of the second prototype after the copper was etched in an acid bath.

The design in Figure 3.1 was made to closely resemble an already-existing breadboard prototype that was known to work, with good stability characteristics (that is, the gain could be set relatively high without causing feedback oscillations). Since unwanted feedback oscillations, analyzed in Chapter 4, depend sensitively on the placement of wires and components, it was expected that a similar board design would have similar stability characteristics.

After installing components and connecting batteries and the Arduino microcontroller, the spectrometer took the form shown in Figure 3.3. This device was connected to a shielded T/R coil, surrounded by a polarization coil and various metal objects carefully located to improve the Earth's magnetic field homogeneity in the inhomogeneous environment of the laboratory.

The gain in the first stage of the receiver has an effective maximum value, above which

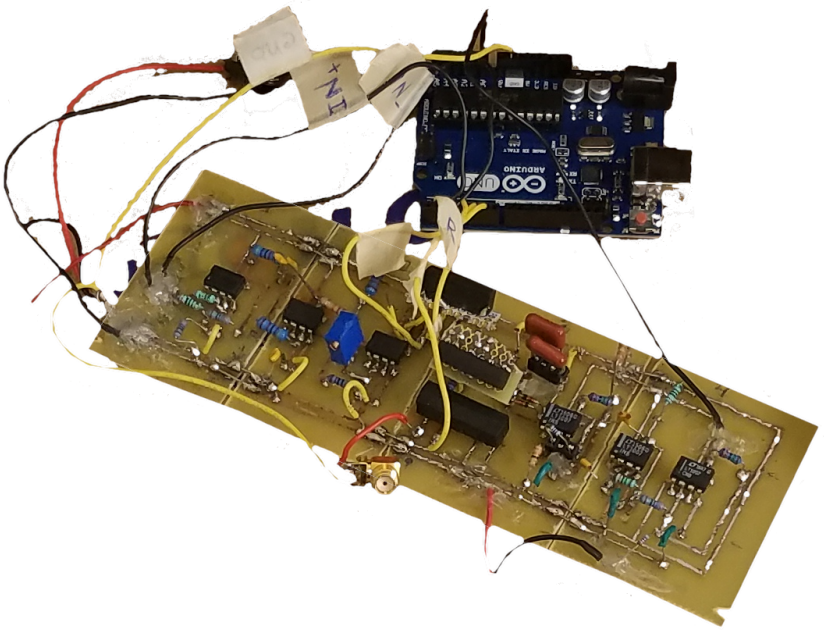

FIGURE 3.3: The lab-printed circuit board (assembled from four individual segments) with a connected Arduino Uno.

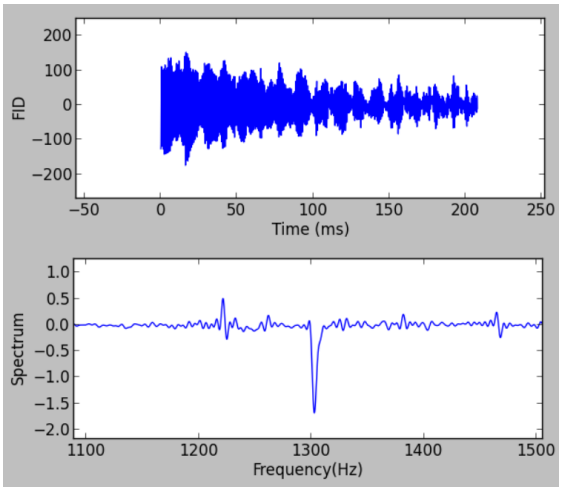

FIGURE 3.4: Well-shimmed result of FID experiment using Prototype II obtained inside the laboratory.

feedback oscillations start to occur. For the lab printed board, this first stage gain is about 270. This is smaller than the 1000-fold gain reported in Michal [10], or the 450-fold gain in the breadboard circuit. However, the gain is still high enough for easy detection of the NMR signal, as shown in Figure 3.4.

Unfortunately, the densely-packed surface mount components are especially difficult to remove and replace. Faulty op amps and relays, among other issues, are a common roadblock when using the spectrometer, so the difficulty of repair makes long-term use less practical.

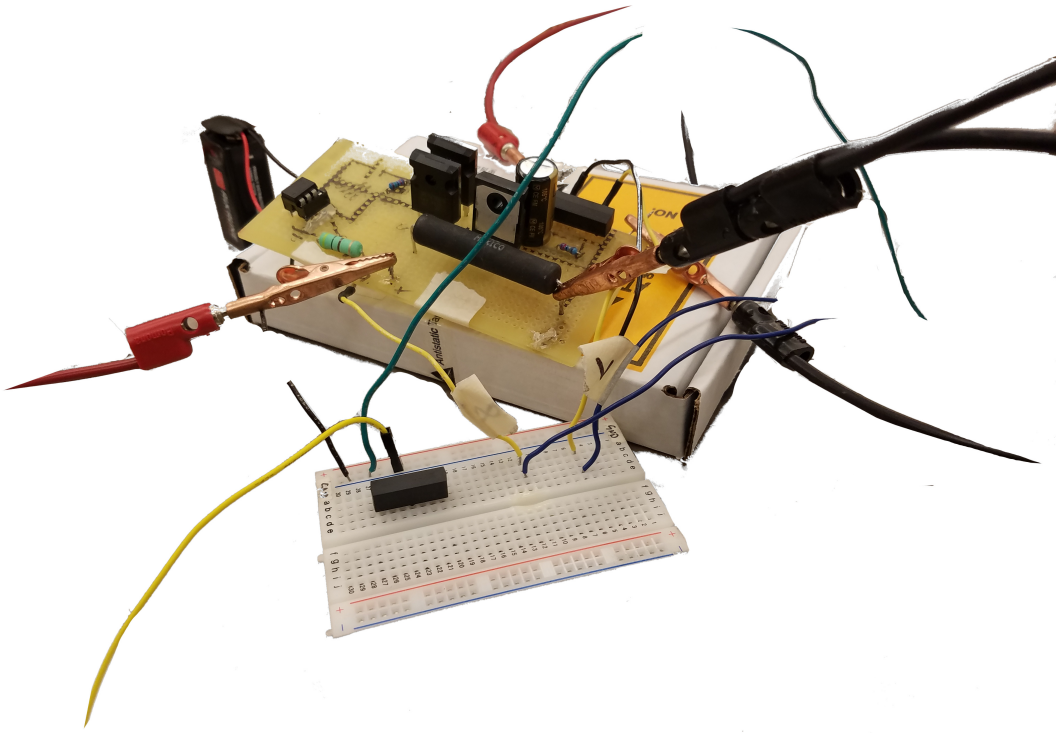

FIGURE 3.5: The polarizer (top) and gradient (bottom) circuits.

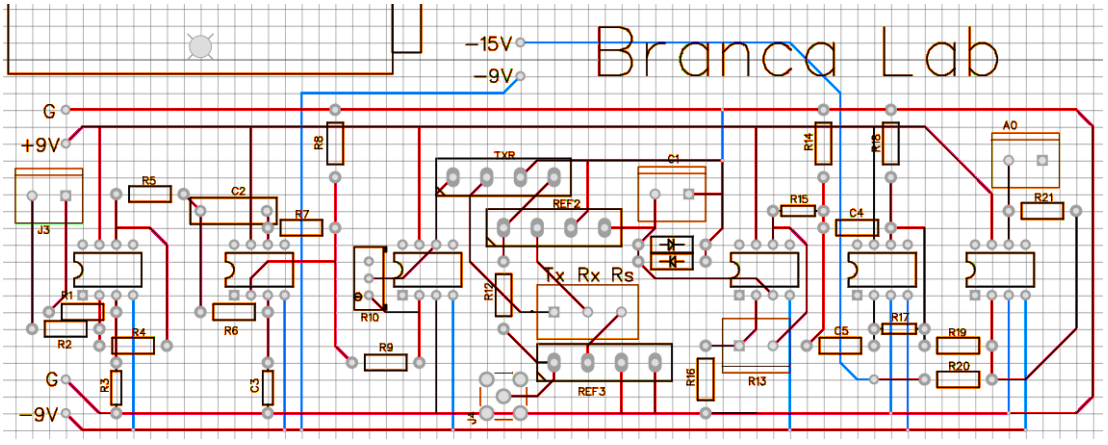

FIGURE 3.6: An image of the professionally-manufactured PCB design in EasyEDA. Red traces appear on the top layer and blue traces on the bottom layer.

The circuits controlling the polarizing coils and gradient coils were constructed using breadboards, since the design is relatively simple and easy to replicate. The breadboards used for this purpose are shown in Figure 3.5.

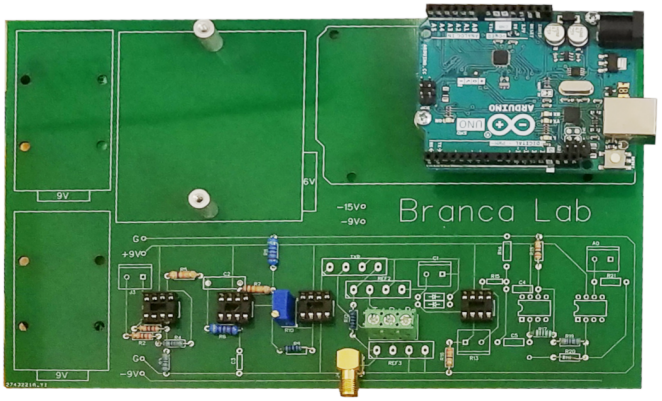

FIGURE 3.7: The professionally-manufactured PCB, with some components installed. To minimize material damage to connecting wires, the Arduino and batteries (not shown) can be screwed securely onto the board. The PCB can hold either an Arduino Uno or Mega.

3.2 Professionally-Printed Board

To ensure the long-term durability and reliability of the spectrometer, a second prototype was built with a professionally-printed board (see Figure 3.6 and 3.7). Because battery packs were connected to the first PCB with loose wires, and not secured in place, frequent use of the board caused the wires to bend and eventually break. The second prototype has space to mount the batteries and Arduino on the same board as the transmitter and receiver. Other common stress points of the previous design, including the SMA connector, potentiometer, tuning capacitor socket, and others were all secured more firmly in the second PCB.

3.3 Calibration of Bc Frequency and Duration

To test the spectrometer, a simple experimental procedure was followed. Inside the laboratory, the field strength was measured with the magnetic probe to be 30 μT with limited precision (uncertainty $\pm$ 2 μT). As a result, the resonant frequency ω_L was known with an uncertainty of $\pm$ 200 Hz. Detection of a signal at ω_L was possible as long as the frequency of $\mathbf{B}_c$ was close enough to the resonant frequency ω_L.

Data was collected and visualized to look for signs of a promising FID spectrum. For each test run, an additional period of data collection occurred with the polarizer turned off. This control test identified which peaks in the spectrum were due to noise and which may have been due to an NMR signal. Once a signal consistently appeared in the

trial but not the control, we were able to refine the estimation of B_0 and the supplied frequency of $\mathbf{B}_c$.

The ideal transmitter strength was also not known, so $\mathbf{B}_c$ duration was varied in addition to frequency. Inside the laboratory, a waveform duration of 6 half-cycles (with $V_T = 1$ V) consistently yielded a strong signal, so most experiments were conducted with this setting. The exception was an outdoor experiment described in the Variation of $\mathbf{B}_c$ Duration section.

3.4 Shimming of Earth's Field and Gradient Coil Tests

In the free-induction decay experiment, the quality of the spectrometer data is partially determined by the linewidth of the peak in the signal spectrum. This linewidth is dependent on the homogeneity of the external magnetic field. Any spatial variation in the magnetic field will cause dipoles in different regions of the sample to precess at different rates, creating a range of frequencies rather than a uniform response.

Although the Earth's magnetic field provides a very homogeneous magnetic field in the absence of human activity, indoor locations such as laboratories typically have large spatial variations in the ambient field. To make laboratory Earth-field experiments practical, one can introduce additional disturbances to the magnetic field to cancel out the variation already present. In NMR, the practice of adding small magnetic fields to even out B_0 is known as shimming. There are two principal types of shimming: active and passive. Active shimming uses an electromagnet or ferromagnetic objects that generate a magnetic field regardless of its surroundings. Passive shimming uses paramagnetic or diamagnetic objects that respond to existing magnetic fields by generating small fields of their own. Passive shimming is typically very simple but makes a smaller impact on the inhomogeneities.

In the laboratory setup, we place several metal objects (screwdrivers and an aerosol can) near the coils for passive shimming. Finding the optimal configuration of objects is a case of trial-and-error. See Figure 3.8.

We also implemented an active shim using the gradient coil. The gradient coil creates a magnetic field that varies approximately linearly along the x direction. The results of the active shimming experiment are included in the Active Shimming section. This experiment also served as validation for the gradient coil functionality. For active shimming, the current through the gradient coils is adjusted to be very low, less than 0.1 mA. To operate the one-dimensional imager, we use larger currents, widening the spectral peaks as far as possible while keeping the SNR high.

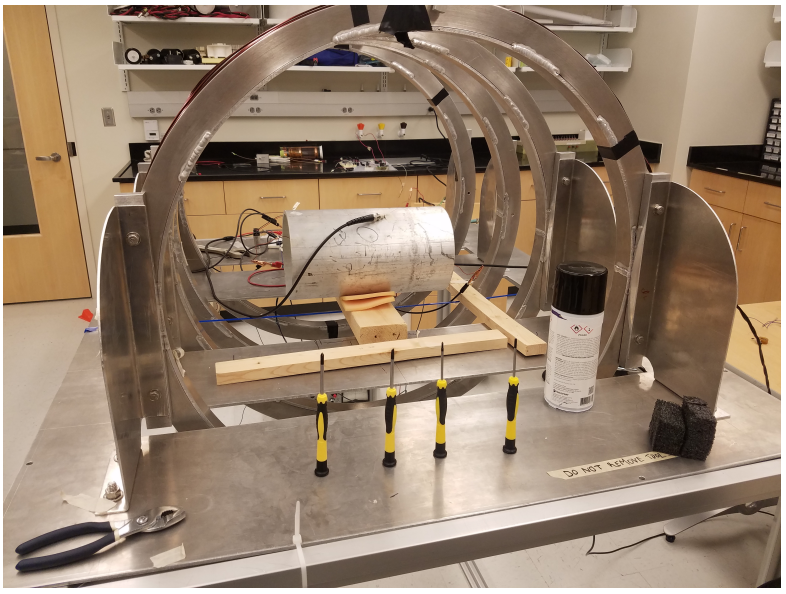

FIGURE 3.8: Aerosol can and screwdrivers used for passive shimming.

3.5 Change in Inductance from Shielding

To reduce the interference of ambient electrical signals with the T/R coil, a segment of large aluminum tubing is used as shielding. This shield contains not only T/R coil, but also the gradient and polarization coils. Note that the introduction of the shielding changes the inductance of the coil. As the coil generates an oscillating magnetic field, electric currents are induced in the conductive shielding, which in turn generate their own magnetic fields that may be picked up by the receiver. When tuning the circuit, it is important to recheck the inductance of the coil with the shielding in place.

The ability of the shielding to reduce ambient noise is significant and clearly visible in Figures 3.9.

3.6 Pre-Polarization of Nuclear Spins

Although the polarization coil is a simple and reliable way to polarize the spins, it does add complexity to the design that may make initial debugging more difficult. To simplify the prototyping processes, we use a large permanent magnet as a temporary spin polarizer. The device consists of two neodymium rare-earth magnets attached to two metal walls spaced about 10 cm apart. The magnetic field strength in the region between the two magnets is about 0.2 Tesla. The water sample polarizes in about 20 seconds. To conduct the experiments, the sample is placed next to the permanent

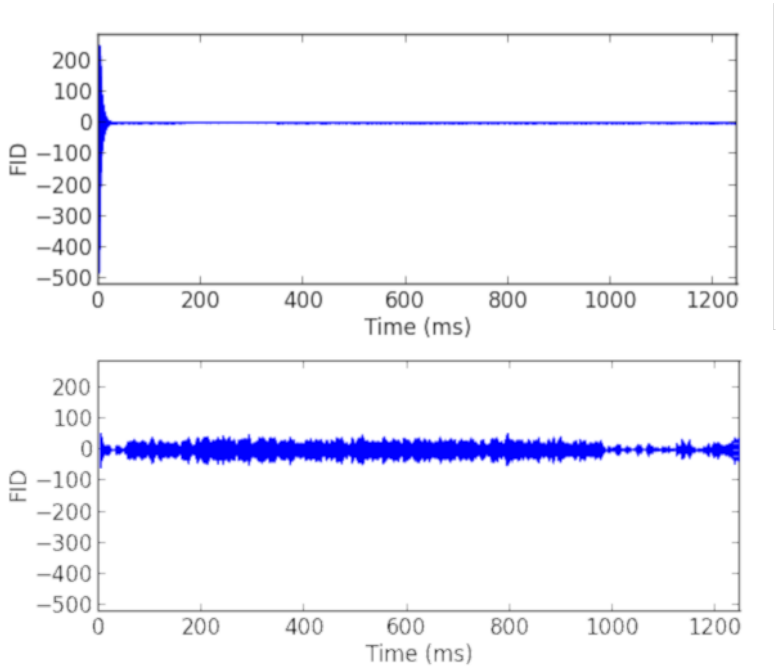

FIGURE 3.9: Top: typical test run, with a shielded T/R coil. Bottom: same experiment as top, but without the shielding in place.

magnet for 20 seconds. Then it is quickly removed from the magnets and placed into the T/R coil before the polarization wears off.

3.7 Compatibility of Arduino Uno and Arduino Mega

Michal's design calls for an Arduino Duemilanove microcontroller. We use the very similar Arduino Uno for the spectrometer and experience no compatibility issues. Since the Arduino Uno's limited memory can pose a significant restraint on the complexity of modifications to the default code, we tested the compatibility of a larger cousin of the Uno, the Arduino Mega. A slight modification must be made to the code location

```
sbi(PRR,PRTWI);
sbi(PRR,PRSPIc);
```

in the script "ArduinoCode". Here **PRR** refers to the Power Reduction Register - the Uno has only one, but the Mega has two. Therefore, replacing the above code with

```
sbi(PRR0,PRTWI);
sbi(PRR0,PRSPIc);
sbi(PRR1,PRTWI);
sbi(PRR1,PRSPIc);
```

activates the power reduction command on the Mega. This is the only compatibility issue. We successfully used a version of the code, larger than the maximum program size of the Uno, with the Arduino Mega.

3.8 Outdoor Experiments

After initial experiments in the laboratory, field experiments were conducted in Battle Park, a forest located near the UNC campus. The park contains large patches of undeveloped land hundreds of meters from power lines, buildings, or vehicles. The absence of overhead power lines is a particularly important criterion for choosing an EFNMR experiment location. Figure 3.10 shows the time-domain signal of a control experiment (with no sample) conducted about 30 meters from a typical medium-voltage power line. The sensitive PCB electronics picked up many frequencies from the large AC current in the power line, leading to a large output signal that somewhat resembles a real FID signal. The significance of the power line interference demonstrates that an ideal experimental location will be at least several hundred meters from power lines.

A photograph of an FID experiment conducted in the forest is provided in Figure 3.11. The coordinates of the experiment location are 39.914028 N and 79.042140 W.

To conduct the outdoor experiment, a portable power supply is required for the polarization coil. We use a 6V lead-acid battery attached in place of the wall power supply. For manual polarization we also bring the neodymium magnet to the experiment site.

3.9 Active Shimming

Under conditions where feedback oscillations do not affect the signal acquisition, we measure the effect of small gradient fields on the NMR linewidth. Since the frequency resolution of the spectra is low, we cannot directly obtain the linewidths. Instead, we assume that the signal strength S (defined in Equation 3.1) is the same in each measurement. This assumption follows from the fact that the transmitted field $\mathbf{B}_c$ is kept at constant strength and duration, and the polarization strength is also held constant. Based on Equation 3.1, if the width of the signal increases but S remains the same, the average value of the signal spectrum $\hat{F}(\omega)$ decreases. We assume each spectral peak has approximately the same shape, so that the average value of the peak is proportional to its maximum value. Therefore, we record for the maximum value in the spectrum as a proxy for linewidth. Higher maximum value indicates narrower linewidth. The results of the active shimming experiment are shown in Figure 3.12. In

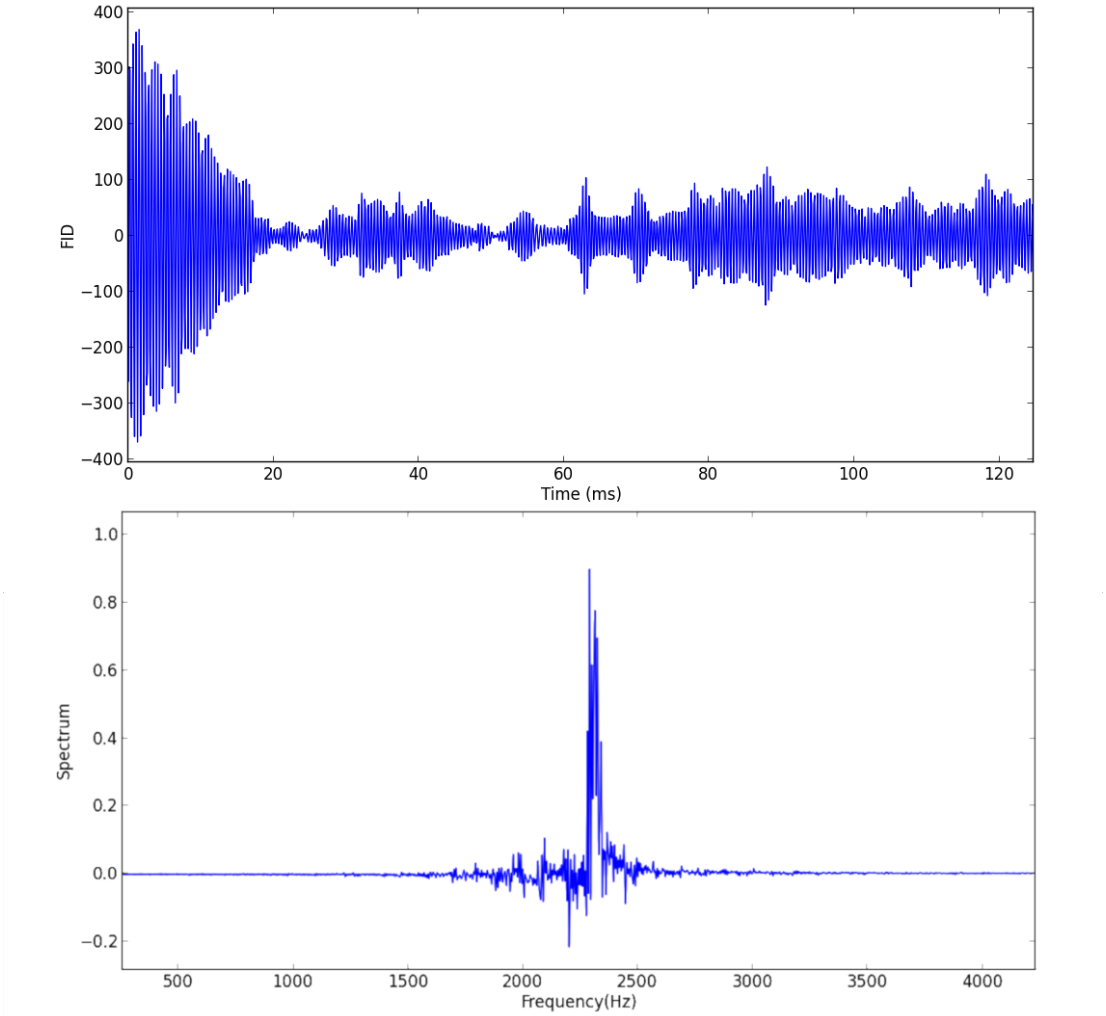

FIGURE 3.10: Time-domain (top) and spectral-domain (bottom) data from a control experiment with a large spurious signal generated from nearby power lines.

these experiments, different resistors were used to change the current in the gradient coil. For each resistor, the resulting spectral maximum was measured and plotted as a function of the inverse of the resistance, which is proportional to the current and therefore a proxy for the strength of the gradient magnetic field.

3.10 Linewidth

The limited resolution of the collected spectral data prevents a precise measurement of the linewidths, but we can place bounds on linewidth to compare the NMR signal characteristics under outdoor and indoor conditions. We refer to the spectral resolution as $\Delta\omega$. We bound the full-width-half-maximum (FWHM) measure of linewidth by

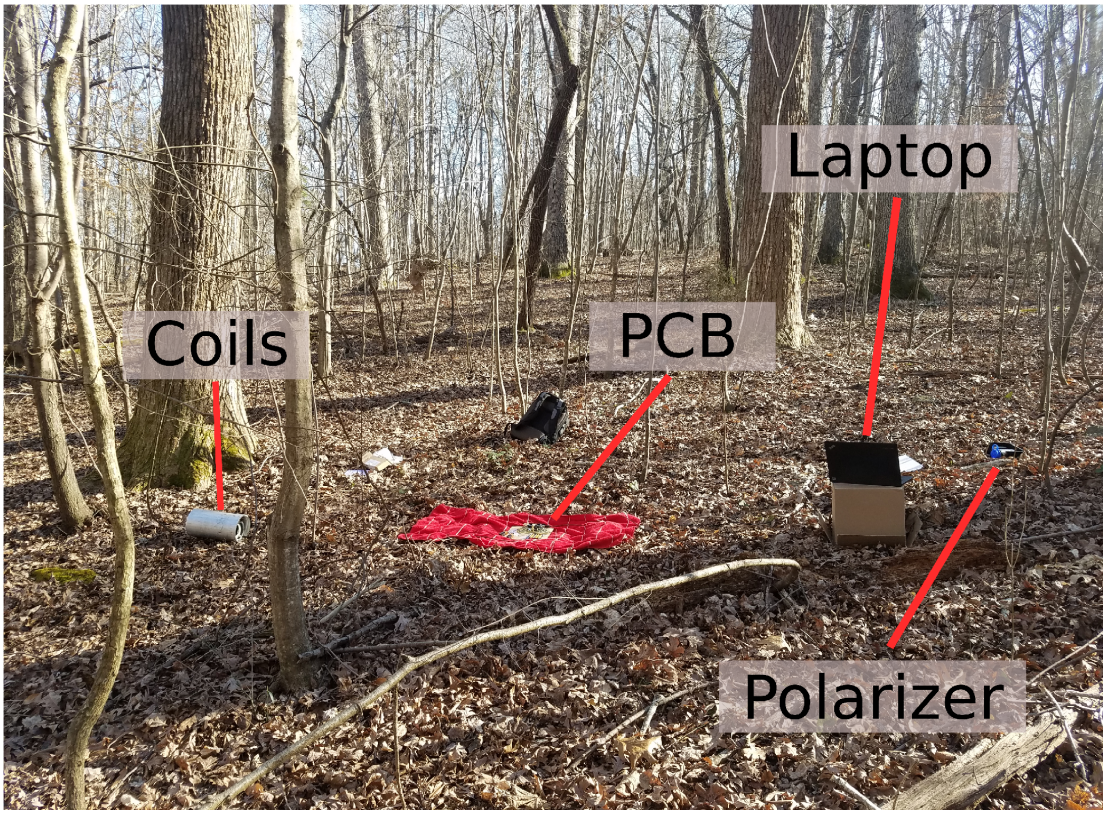

FIGURE 3.11: Outdoor experimental setup. In this example, the permanent magnet is used to polarize the sample. Note that the polarizer magnet must be kept several meters from the coils to prevent interference with the Earth's magnetic field at the location of the coils.

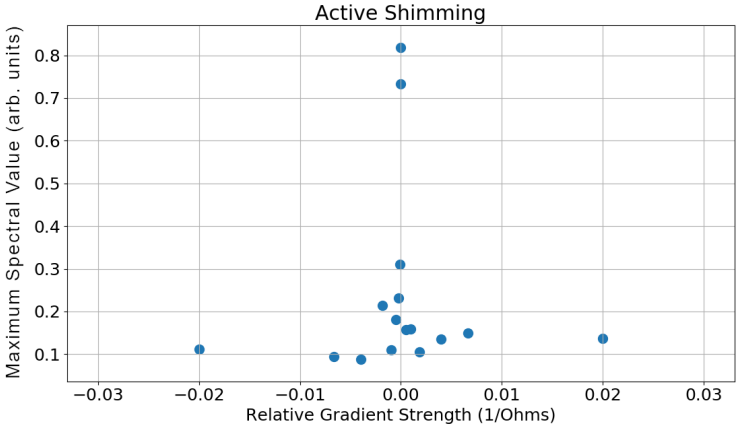

FIGURE 3.12: The relation of maximum spectral value with relative gradient magnetic field strength.

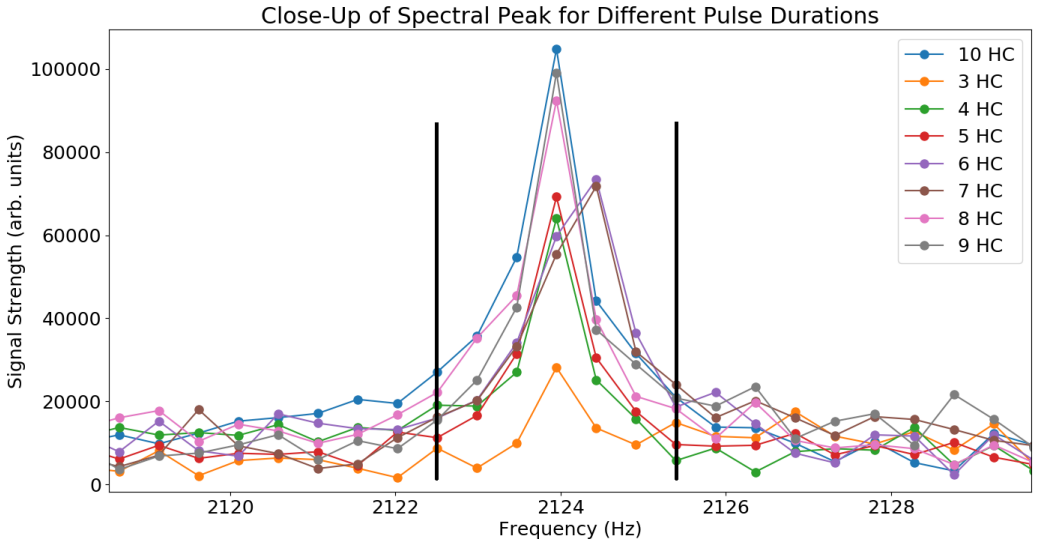

FIGURE 3.13: A closeup of the spectra for several measurements taken with different $\mathbf{B}_c$ durations or half-cycles (HC). The integration range for the signal strength calculation is shown by the two black lines (from 2122.5 Hz to 2125.5 Hz).

counting the number of spectral support points N_ω in the peak located above one-half of the maximal value. The upper bound on linewidth is $\Delta\omega(N_\omega + 1)$, and the lower bound is $\Delta\omega(N_\omega - 1)$. Using this method, we calculate that the narrowest linewidth achieved inside the laboratory is 16 $\pm$ 8 Hz. Because the smallest N_ω for the spectra collected outside is 1, we cannot define a lower bound. We report that the linewidth is less than 0.96 Hz.

3.11 Variation of Bc Duration

To check that the $\mathbf{B}_c$ duration was optimized for maximum signal strength, we varied the $\mathbf{B}_c$ duration, measured by integer number of half-cycles. In this experiment it was valuable to maximize SNR so the variation of signal strength was most apparent and least affected by noise. In this case the optimal setup was the outdoor experiment with manual polarization, which demonstrated the largest and sharpest spectral peaks.

To calculate the signal strength we determine a range of frequencies spanning the width at the base of the peak (see Figure 3.13). Because the spectral signal $\hat{F}(\omega)$ is present across a small range of frequencies, we define the signal strength S to be a sum of each frequency's contribution

$$S = \int_{\omega_a}^{\omega_b} \hat{F}(\omega) d\omega \tag{3.1}$$

such that the peak is present on the interval $[\omega_a, \omega_b]$.

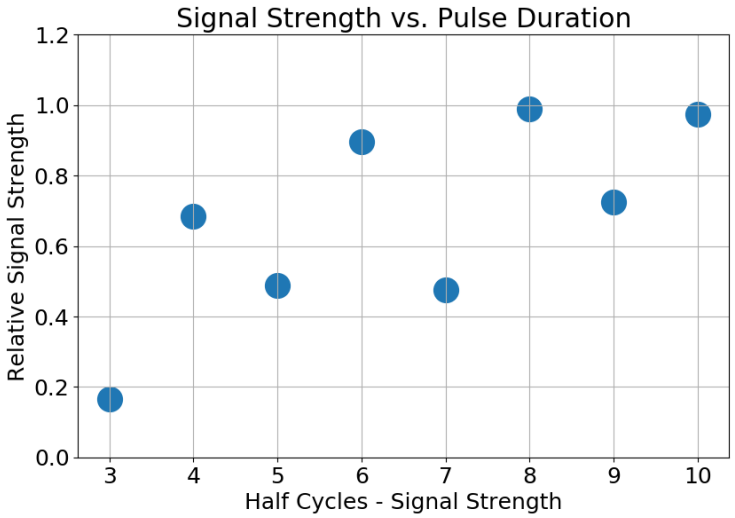

FIGURE 3.14: Variation of signal strength with $\mathbf{B}_c$ duration, measured outside.

We display the observed variation in Figure 3.14. We note a maximum response at 8 half-cycles, and record a significantly stronger signal whenever the number of half-cycles is even (i.e., the $\mathbf{B}_c$ duration is an integer multiple of the period $1/\omega_L$). All measurements were taken with a V_T 1 V. Varying this amplitude might change the optimal $\mathbf{B}_c$ duration.

Chapter 4

Hardware Performance

Throughout the course of experiments, both PCBs were plagued with feedback oscillations. The feedback oscillations are characterized by a large signal greater than the maximum voltages that the op amps can supply and a frequency equal to that of the bandpass filter frequency. The term "feedback oscillation" refers to the fact that they typically occur when the gain of the receiver is set too high, as if some feedback mechanism causes the highly sensitive output of the amplifiers to couple back into the input and become unstable. The oscillations completely erase any readable signal and persist even after the signal has finished.

Some observed features of the feedback oscillations make it difficult to explain what the coupling mechanism is. In the following section, we outline experiments and tests that helped to characterize the nature of the feedback oscillations.

4.1 Hysteresis

Hysteresis is the property of a physical system to behave according to rules based on past states, not just the current state. The feedback oscillations exhibit hysteresis with respect to the variable gain on the first amplification stage. To demonstrate this, we replace the 330 kOhm resistor with a potentiometer. We feed a continuous small signal from a function generator into the receiver. Increasing the potentiometer from a small value P, and thus increasing the gain, we first observe feedback oscillations begin at $P = P_0$. Then we decrease the potentiometer value below P_0, and the oscillations persist. Only after we lower the potentiometer to some other value P_1 do the oscillations cease (see Figure 4.1).

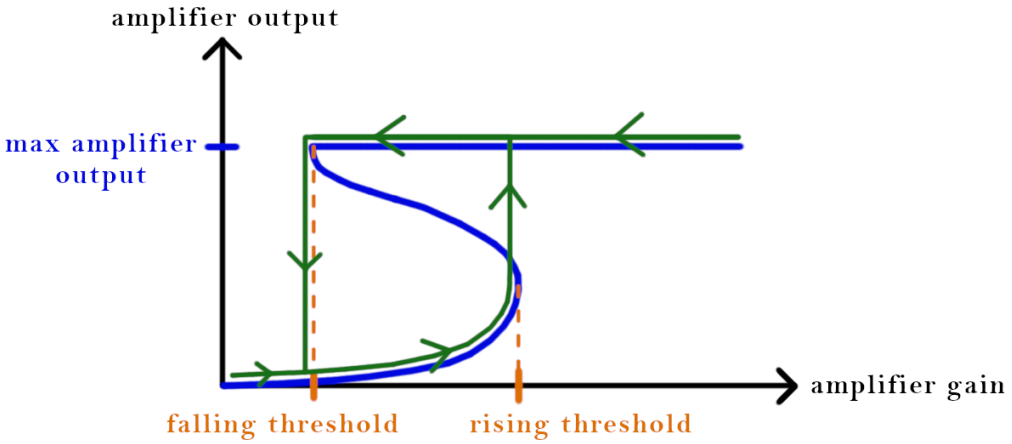

FIGURE 4.1: A qualitative sketch of the relationship between gain and feedback oscillations. Gain must be reduced to much lower than the unstable threshold to return the receiver to a normal state. In effect, there are two different thresholds: a "rising threshold", the point at which an increasing gain initiates the oscillation, and a "falling threshold", the point at which a decreasing gain no longer supports the oscillation. The rising threshold exceeds the falling by a factor of about 3.

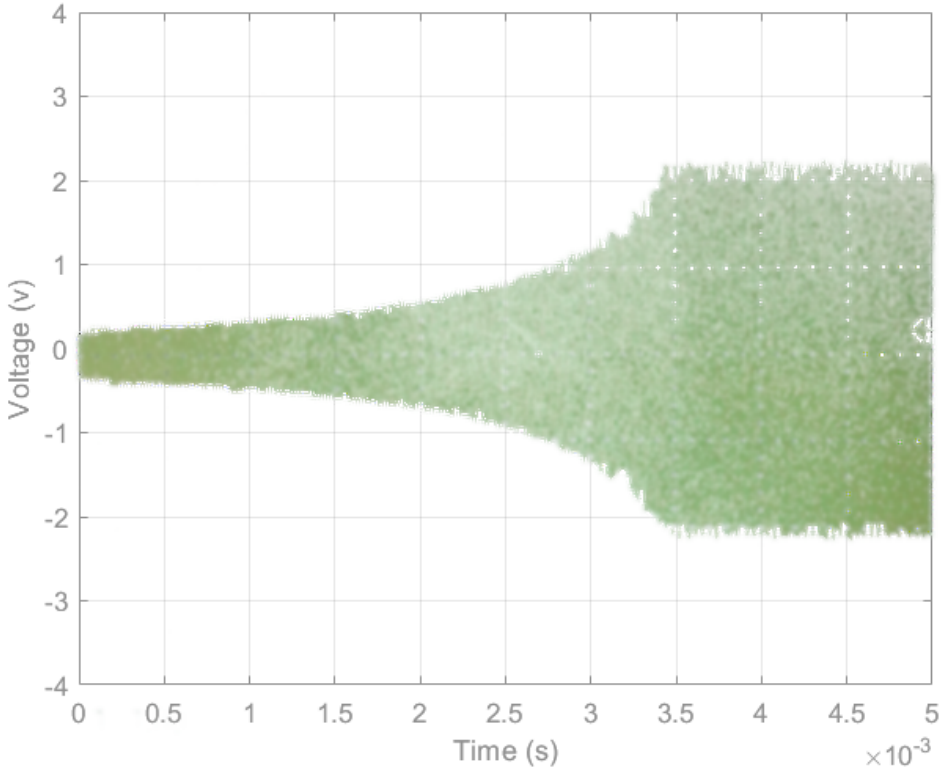

FIGURE 4.2: This oscilloscope data shows the onset of a feedback oscillation, just as the gain passes a certain threshold. This feedback oscillation exhibits hysteresis, as described in Figure 4.1.

4.2 Effect of PCB Design on Feedback Oscillations

The professionally-printed circuit board fared much worse with respect to feedback oscillations than the lab-printed board. The typical max-gain-before-oscillation of the lab PCB is about 14000, but only 2200 for the professional board. In the latter case with this small gain the SNR becomes too low and NMR spectroscopy is no longer practical. The two boards were designed to have nearly indentical component layouts and similar wire paths (see Figures 3.1 and 3.6). The primary difference between the two is that the power for the pull-up resistor (two AA batteries) are connected via a wire that runs underneath the second stage of the receiver amplifier (as opposed to away from the board entirely). This design choice aimed to keep the board compact and reduce the number of jumper wires dangling above sensitive components. However, it may have had a serious negative effect on the stability of the professional board.

Another significant difference in the two boards is the placement of ground wires. Both boards have two common ground wires that run above and below the components in a straight line. On the lab board, these ground wires are only connected by a wire on the receiver end of the PCB. On the professional board, the ground lines are connected on both ends.

4.3 Effect of Ground Wire Placement

The redundant connection to ground may seem innocuous, but tests with a breadboard version suggest it may be an important factor for causing oscillations. Placing the ground connection wire on the receiver side, as in the lab board, always results in feedback oscillations. On the other hand, placing the wire only on the transmitter side does not cause oscillations. This observation appears to contradict that of the previous section if induced voltages on ground wire connectors are to blame for feedback oscillations. However, the fact that the feedback effect can be controlled with the placement of a seemingly trivial connection points to a coupling effect involving the ground wire.

Another effect relating to the ground wire complicates matters further. On the breadboard spectrometer, if the ground connection to the Arduino is connected to the upper ground rail, no oscillations appear. Oscillations always appear if the ground link to the Arduino is connected to the lower rail.

4.4 Effect of Analog Input Connections on Feedback Oscillations

Regardless of the board, whenever feedback oscillations do occur, they can be observed by connecting the output of the receiver to an oscilloscope. An interesting phenomenon occurs when the receiver output remains connected to the oscilloscope but is disconnected from the microcontroller analog input. This input contains an analog-digital converter that sends voltage data to a computer. Disconnecting this wire prevents the data from being saved. However, it also prevents feedback oscillations. The oscilloscope displays signals that would have been lost otherwise. In fact, the professional PCB is capable of producing high quality NMR signals, as long as it is not sending the signal to the microcontroller. Interestingly, the oscilloscope functions much the same way, in principle, as the microcontroller analog input - it takes in a physical voltage from a wire and generates a digital representation of the voltage value. If the oscilloscope were not so expensive, it could easy replace the Arduino as the data acquisition hub for this spectrometer design. Since the precise input impedance, sample rate, etc. of the Arduino and oscilloscope are not known, we cannot compare the two devices to determine the cause of the discrepancy. Furthermore, the problem is not unique to a particular Arduino - we tested several units including genuine and imitation versions of the Arduino Uno and Mega.

4.5 Test with Unity-Gain Amplifier on Analog Input

One proposed explanation for the behavior of some PCBs when connected to the analog input is that the Arduino input has a low input impedance compared to the oscilloscope. If this were true, the Arduino would draw more current from the output of the receiver. This current then might inductively couple to other parts of the circuit. To test this, we install a unity-gain op amp circuit on the output of the receiver. We place the op amp several inches away from the receiver and connect the amplifier output to the Arduino. We expect that if inductive coupling on the receiver output causes feedback oscillations, the op amp will prevent them because the input resistance is so high. This way, the current leading away from the PCB is negligible and the Arduino still receives the signal. However, this configuration still yielded feedback oscillations. Surprisingly, the unity gain non-inverting op amp configuration caused oscillations even without being connected to the Arduino. This suggests that the effect of the non-inverting op amp on the circuit is similar to that of the Arduino. The significant difference between the non-inverting and inverting amp configurations is that the non-inverting amp has

a connection from the output to ground via a resistor. It is possible that non-zero resistance in the ground wire causes the ground voltage in different parts of the circuit to be slightly different, leading to some electrical feedback effect.

4.6 Test with Second Microcontroller

Since the goal of the device is low-cost spectroscopy, we attempt to use another Arduino for the sole purpose of reading voltages in the hopes that the feedback mechanism would decouple. To do this, we write Arduino code that stores voltage data when triggered by another Arduino. This allows one Arduino to control the operation of the experiment while the other stored FID data. However, in order for this configuration to work, the ground voltage of both Arduinos needs to be the same. Otherwise, floating voltage offset will make the output of the receiver unreadable to the 0 to 5 volt analog pin. However, anytime the grounds of the two microcontrollers are connected and the output of the receiver is connected to either Arduino, feedback oscillations result. This is true whether the microcontrollers are connected to the same laptop or to two different ones.

4.7 Initiation Timing of Feedback Oscillations

Critical to the understanding of the feedback oscillations is the initiation timing. Since different control signals occur at different times, observing the beginning of a feedback oscillation may pinpoint the source. Observing the output of the receiver with an oscilloscope, we see that the oscillations begin at time τ_1 (referring to Figure 2.3), corresponding to the receive short command where the T/R coil is grounded. However, if we unplug the wire delivering that command, feedback oscillations are initiated anyway at time τ_2, when the receiver opens. This suggests that any sudden shift in voltage triggers the oscillations. In normal experiments, we observe a characteristic "ring-down" of the T/R coil as the receiver opens. The signal on the output during this ring-down phase often reaches the power rails.

4.8 Other Observations

- The likelihood of feedback oscillations seems to be also location-dependent. The same board with the same parameters can exhibit oscillations one day and not the next. While performing experiments outside, the gain usually had to be lowered by about half to prevent oscillations. This may suggest inductive coupling as the

culprit, since the induced voltage increases proportionally to the frequency, and the ambient magnetic field outside required twice the $\mathbf{B}_c$ frequency as the field inside the lab.

- We can connect the analog input of the microcontroller to various stages of the circuit, not just the final one. Connecting the output of the second amplification stage results in feedback oscillations only triggered by the opening of the receiver (not the receive short command) and they disappear when the receiver is closed, unlike the normal oscillations. Connecting to the output of the first stage gives no oscillations, and the input of the first state looks just like the output of the second stage.

Chapter 5

Parasitic Inductance Analysis

From Maxwell's equations, we can formulate a model for the unwanted electromagnetic coupling between different parts of circuit boards. Specifically, as the NMR signal drives a small AC current through the components of the PCB, oscillating magnetic fields are created. These fields can induce unwanted voltages in nearby components. Although for low-frequency applications these "parasitic inductance" effects do not generate appreciable voltages, the large gain of the receiver amplifiers make them extremely sensitive to coupling effects.

In this analysis we create a two-dimensional model of the receiver on the lab-printed circuit board that captures most of the conductive elements. Using a numerical integration technique, we find the coupling strength between each component and wire trace on the PCB. We use the coupling model to identify problematic areas or components that generate or amplify unwanted induced voltages. Although the model is crude and not designed for quantitative determination of maximum possible gain, for example, it does inform certain guidelines and strategies to mitigate parasitic inductance.

5.1 Theoretical Framework

We start with the equation known as Faraday's Law [11]

$$\nabla \times \mathbf{E} = -\frac{\partial \mathbf{B}}{\partial t} \tag{5.1}$$

and the equation known as Ampere's Law

$$\nabla \times \mathbf{B} = \mu_0 \left(\mathbf{J} + \epsilon_0 \frac{\partial \mathbf{E}}{\partial t} \right) \tag{5.2}$$

We opt to neglect the second term on the right side of Ampere's Law. The reason for this choice is that this term represents a coupling between in electric and magnetic fields that gives rise to electromagnetic radiation. In electronics for conventional NMR, EM radiation is a major source of noise generation and a key focus of electromagnetic interference (EMI) analysis. [12] However, the energy radiated away by EM waves is inversely proportional to the square of the signal frequency. [11] As the frequency of the signals generated in our circuit is only 1-2 kHz, the time derivative of the electric field is small. In other words, we do not analyze "antenna-like" behavior of the components, but only mutual inductance effects.

We take the curl of Equations 5.1 and 5.2 to see that

$$\nabla \times (\nabla \times \mathbf{E}) = -\frac{\partial(\nabla \times \mathbf{B})}{\partial t} = -\mu_0 \frac{\partial \mathbf{J}}{\partial t} \tag{5.3}$$

We can use the curl-curl vector identity [11], $\nabla \times (\nabla \times \mathbf{E}) = \nabla(\nabla \cdot \mathbf{E}) - \nabla^2 \mathbf{E}$, to simplify. We are not interested in buildup of electric charge, so by Gauss' Law, the divergence $\nabla \cdot \mathbf{E}$ is zero. The problem turns into three separate Poisson equations.

$$\nabla^2 \mathbf{E} = \mu_0 \frac{\partial \mathbf{J}}{\partial t} \tag{5.4}$$

where ∇^2 is the vector Laplacian operator. From this equation, we can see that induced electric fields are always parallel to the change in current.

In this analysis, we consider all components to be contained in a two-dimensional x-y plane, which simplifies the calculations greatly. Since no current flows in the z direction, the electric field has no z-component as well. We note that the two-dimensional assumption neglects the three-dimensional shape of capacitors, jumper wires, and other components that extend above the surface of the PCB. Also neglected are the inductive effects of the operational amplifiers, relays, and terminal blocks.

After solving Equation 5.4, one can find the induced voltage in an electronic component with the following integral

$$\varepsilon = -\oint_{\mathcal{C}} \mathbf{E} \cdot d\mathbf{l} \tag{5.5}$$

where $\mathcal{C}$ is some curve in the x-y plane. In our analysis $\mathcal{C}$ always follows paths representing wires on the PCB. Combining Equations 5.4 and 5.5, we can, in principle, determine the induced voltage ε on a wire defined by $\mathcal{C}$ due to an arbitrary changing current density $\mathbf{J}$. This allows us to estimate the inductive coupling effects among wires. In the next section we describe a method of implementing a simulation using this framework.

5.2 Numerical Implementation

We divide the simulated PCB into a grid of discrete points with separation dx. All of the wires point along either the x direction or the y direction, so the induced electric field is also either pointing along $\hat{i}$ or $\hat{j}$, never diagonal. This has an important consequence: a varying current pointing in the x direction cannot induce a voltage in a y-pointing wire, as Equation 5.4 is made from three fully independent equations.

Suppose that we have two wire elements A and B broken into i and j number of cubes of side length dx (refer to Figure 5.1). Let us refer to the position of cube A_i as $\mathbf{r}_i$ and of cube B_j as $\mathbf{r}'_j$. Wire A carries a current density $\mathbf{J}$. The desired quantity is the electric field $\mathbf{E}_j$ at point $\mathbf{r}'_j$ due to $\mathbf{J}_i$ at point $\mathbf{r}_i$. We approximate the cube A_i as a point current source. Then the solution to the Poisson equation has well-known form (based on Gauss' Law) [11]

$$\mathbf{E}_i = \frac{\mu_0}{4\pi|\mathbf{r} - \mathbf{r}'|} \int_{\mathcal{V}} \partial_t \mathbf{J}_i dV \tag{5.6}$$

where $\mathcal{V}$ is a volume. Since $\partial_t \mathbf{J}_i$ is constant within the discretize cube, the integral is just $\partial_t \mathbf{J}_i dx^3$, or $\partial_t \mathbf{I}_i dx$.

We note that the Laplacian is a linear operator. That is, the electric field caused by the sum of many current elements is the same as the sum of many electric fields caused by single current elements. Thus, we can sum the electric fields caused by each A_i to get the total field on B_j induced by A.

The next step is to calculate the voltage along the entirety of B. We can discretize Equation 5.5 to get

$$\varepsilon_B = -\sum_j \mathbf{E}_j dx \tag{5.7}$$

We can now define the coupling constant M_{AB} as the voltage induced on wire B per change in current over time.

$$M_{AB} = \sum_i \sum_j \frac{\mu_0}{4\pi|\mathbf{r}_i - \mathbf{r}'_j|} dx^2 \tag{5.8}$$

such that

$$\varepsilon_B = -M_{AB} \frac{\partial}{\partial t} I_A \tag{5.9}$$

for any wire elements A and B.

A similar numerical technique for calculating mutually induced currents in PCBs is described by Sonntag et. al. [12]. Their model is based on the Neumann formula of

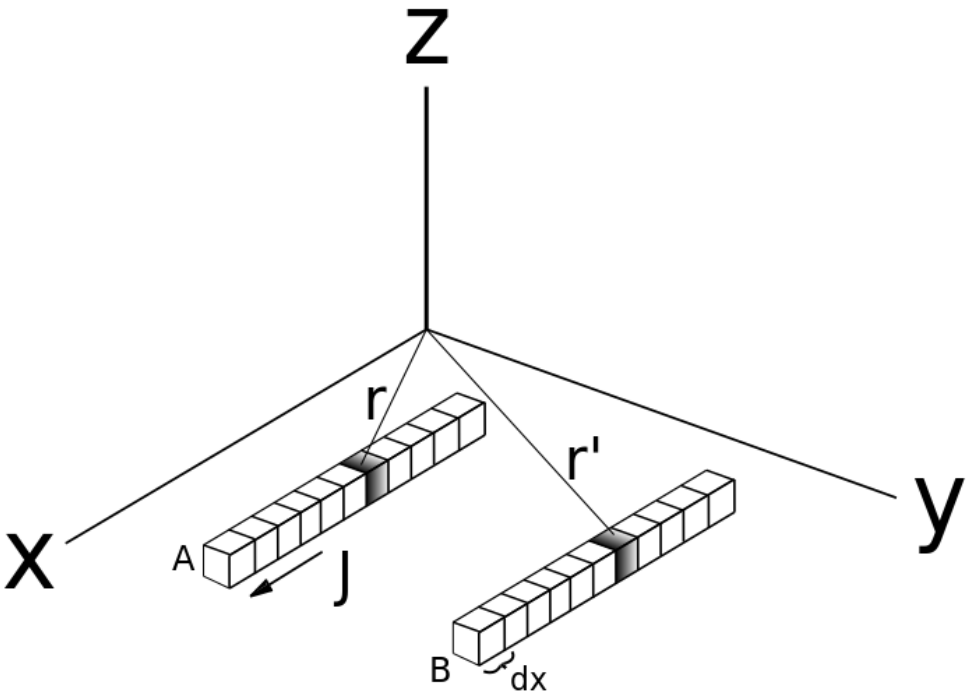

FIGURE 5.1: Illustration of the numerical simulation principle.

mutual inductance and allows for more complicated wire geometries, including three-dimensional traces.

To put this analysis to practice, we manually designate the regions of the PCB where current flows and the direction of the flow, as shown in Figure 5.2. We also need the currents I_A to determine ε_B. Of course, these currents are in turn dependent on the voltages ε_B, and a full time-dependent simulation of the PCB would take this into account. However, we are interested in the general question of whether magnetic induction plays a role in feedback oscillations. Therefore we only need to check whether the induced voltages are large enough to have a significant impact on performance. To this end, we use the transient circuit simulator in the free LTSPICE software to find the current through all receiver wires in the circuit under normal operation (see Figure 5.3). Normal operation is defined to be a small input to the receiver such that the output has about 1 V amplitude (a typical signal size) with a total receiver gain of about 50,000 (the gain used by Michal which is about three times the maximum allowable gain observed in the lab-printed board).

The simulation codes assigns a current value to each corresponding wire element, with the correct direction. Then all the coupling constants M_{AB} are calculated and multiplied with I_A to obtain all induced voltages ε_B. We note that we do not take phase differences

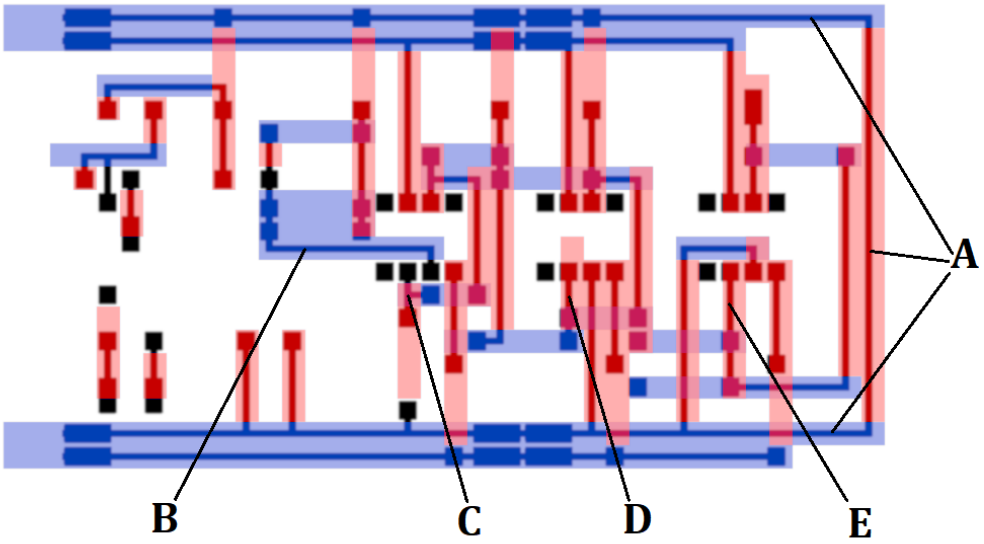

FIGURE 5.2: Manually entered locations of current on top of the outline of the receiver traces. Blue indicates horizontal current and red indicates vertical. Note that the colored areas do not always correspond to the outline because components such as resistors also carry current. The letter labels refer to Table 5.3.

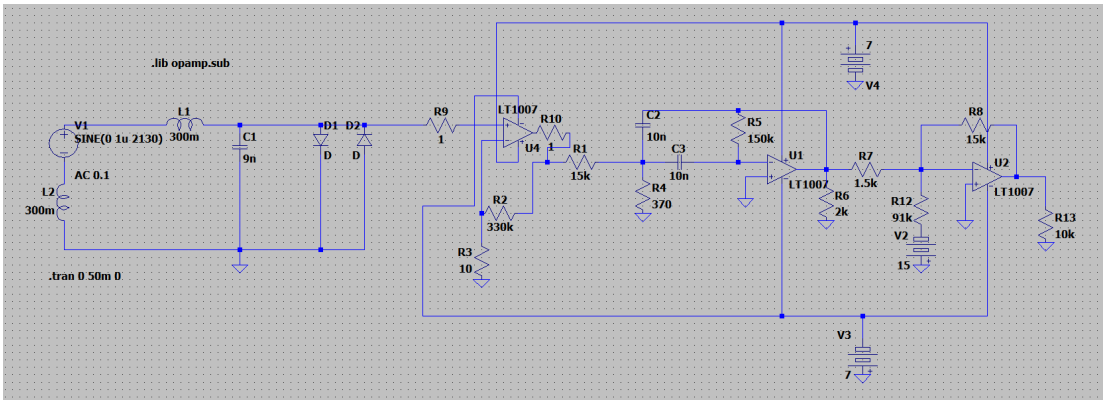

FIGURE 5.3: The LTSPICE simulation used to determine the currents I_A. Note that not all component values shown here were used in the simulation.

in the signal and induced voltages. A phase difference could reduce or reverse the coupling effect. However, by summing all the induced voltages as if they were in phase, we obtain an upper bound on the total induction effect.

In Appendix A, we step through an analytical test case of this simulation and confirm it has validity in at least some circumstances.

Wire Component	Label	Total Induced Voltage (nV)
Ground Loop	A	140
Amp 1 Positive Input	B	14
Amp 1 Negative Input	C	9.7
Amp 2 Negative Input	D	12
Amp 3 Negative Input	E	44

TABLE 5.1: The induced voltages for key components, with normal operating conditions at 50,000 gain. The labels refer to Figure 5.2.

5.3 Results

We defined 57 wire elements in the circuit board. Most wires had induced voltages of a few nanovolts. While our time-independent analysis cannot precisely predict how the signal evolves, it can point to problematic areas in the PCB and suggest possible mitigation strategies.

Some areas of the circuit are likely more sensitive to inductive effects than others. For example, small voltages induced on the traces supplying 9 volts to the op amps will likely not have any affect on the board output, since the signal has less than 9 volts amplitude under normal conditions. To narrow the focus of the analysis, we identify specific wires in the circuit that are more likely to drive unwanted feedback behaviors - the loop of wire acting as common ground for all the components, and the input nodes for each of the op amps. We summarize the results in Table 5.3.

The results of the simulation suggest that coupling effects are small for most wire components. Based on LTSPICE simulations, the voltage on the inputs for the op amps used in the real PCBs is about 20 μV. Even the largest induced voltages would change in input voltages by less than 1%. A fully time-dependent simulation, modeling transient voltage signals caused by switching of relays, is necessary to answer whether these small coupling behaviors are large enough to result in feedback oscillations over a long period of time.

Chapter 6

Conclusions

6.1 Feedback Oscillations

The design provided by Michal sometimes yields a working, versatile NMR spectrometer. However, the design can lead to non-functional PCBs, even if they match the design exactly and closely resemble functional PCBs.

We find that the inductive effects generate at most 1% differences in the operating voltage amplitude on sensitive op amp inputs. However, given that many of the features of the real oscillations resemble those expected from coupling effects, (namely, the gain dependence, ability to persist after the signal ends, etc.) we can still use the results of the simulation to make qualitative recommendations for improving the PCB layout. Moving the ground rail further from the other components would require lengthening of other wire traces, but this harm seems to be outweighed by the benefit of reducing coupling on the ground wire. The third stage amplification also seems vulnerable to coupling and perhaps should be isolated physically or through electrical shielding.

6.2 PCB Development

The most successful implementation of Michal's design that we obtained was the breadboard version with loosely attached parts. This board had the highest gain without oscillations and required the the fewest number of repairs. Although the breadboard layout is crude, with many unused conductive strips in the breadboard causing parasitic capacitance and inductance, the loose connections allow rapid reconfiguration if problems do arise. Experiments with the breadboard show that it was fully capable of oscillations even at low gains, provided certain wire placements were shifted. The

clear limitation of the PCB is that, when working with unpredictable electronics, the wire traces cannot be relocated. If PCBs are used, it is imperative to use adjustable components wherever possible. For example, the transmitter gain, bandpass center frequency, and first stage gain can all be made instantly adjustable by replacing resistors with potentiometers or sockets that can hold resistors. Feedback oscillations and noise signals can appear unexpectedly, so versatility is an essential component of practicality.

In the prototyping workflow, PCBs have an important function as robust, permanent copies of a physical design. However, moving to PCBs too early in a prototyping project can stifle the discovery of new solutions, as more time is spent forcing modifications on a rigid, inflexible platform. PCBs also add to the cost of the spectrometer, shifting the end product away from the original goal. Although breadboards are prone to falling apart, the low-cost components ensure that frequent replacements and readjustments justify the breadboard's versatility.

6.3 Experimental Parameters

The huge improvement in the linewidth moving from laboratory conditions (even after careful shimming, passive and active) to outdoor conditions demonstrates the relative ease with which EFNMR experiments may be carried out, under the right conditions. The outdoor environment removes the need for shimming and reduces the chance that the receiver needs to be re-tuned, as the Earth field is largely constant. In this experiment, active shimming did not improve the linewidth, either because the inhomogeneities in the laboratory were not aligned with the axis of the coil or varied nonlinearly on a small scale. The highest signal strengths in Figure 3.12 result from no active shimming. The variation of the $\mathbf{B}_c$ duration in the outdoor experiment suggested that the magnetization reached $\theta = \pi/2$ with eight half-cycles for a V_T of 1 V.

6.4 Note on Unusual Circumstances

We acknowledge that many results demand further investigation. The $\mathbf{B}_c$ duration experiment clearly needed further testing of higher $\mathbf{B}_c$ durations. The induction coupling simulation may have benefited from experimental verification. The sudden shutdown of research labs in March 2020 due to the COVID-19 pandemic unfortunately halted these immediate inquiries.

6.5 Summary

We build and characterize a EFNMR spectrometer with an emphasis on accessibility and cost. The design provided by Michal [10] includes a transmitter and receiver circuit, operated by an Arduino Uno microcontroller, that generate and detect NMR signals. The design was manifested in two PCBs, one lab printed, and one professionally manufactured. Early experimental procedures such as shimming, shielding, and manual polarization were discussed. An option for Arudino Mega compatibility is outlined. The characteristics of the spectrometer design is measured both in the laboratory and in a low-interference location in a city park. Linewidths achieved away from buildings, powerlines, and other source of interference are at least 8 times smaller than measured indoors, leading to adequate spatial resolution for one-dimensional imaging. The impact of active shimming and $\mathbf{B}_c$ duration parameters is investigated. The problematic phenomenon of feedback oscillations is characterized in depth. To explore one explanation of the feedback oscillations, a numerical simulation is formulated that estimates inductive coupling effects in a simplified model of the lab printed PCB. The simulation suggests the coupling effects are small but could play a role. We outline some changes to the existing layout that could mitigate feedback oscillations. Finally, we comment on the usefulness of the design for small-scale, low-cost NMR projects.

Appendix A

Validation of Induction Model

To ensure that the simulation approach outlined in the Parasitic Inductance Analysis chapter is valid, we imagine a simple test case that can be calculated both analytically and using the simulated approach. We find that the results match and the simulation is valid.

We imagine a finite, straight wire of length b, carrying a current $I(t) = I_0 \cos(\omega t)$. Next to the wire is a rectangular loop with length also b, with one side a distance r from the wire, and the other side a distance a (so the width is $a - r$). See Figure A.1. We want to determine the voltage or electromotive force (EMF) ε induced in the loop due to the changing current $I(t)$. We construct the simulation in the same manner as the simulation for the full PCB. We arbitrarily set $r = 1$ cm, $b = 2$ cm, $a = 3$ cm, and $I(t) = \cos(\omega t)$, where $\omega = 1000$ rad/s. The simulation code outputs a coupling coefficient, which we then feed into an LTSPICE component called an arbitrary voltage source. We use this component to couple the current a simulated straight wire to a simulated loop, as shown in Figure A.2. The resulting current is shown in Figure A.3. This induced current passes through a simulated 100 Ohm resistor. From the figure, the simulated induced voltage in the rectangular loop is 2.09 μV.

Next we try to arrive at the same value analytically. Fortunately, with symbolic calculations, we have useful theoretical tools at hand. Namely, formulating the Maxwell equations in integral form yield [11]

$$\oint_{\mathcal{C}} \mathbf{E} \cdot d\mathbf{l} = \varepsilon = -\frac{\partial}{\partial t} \iint_{\Sigma} \mathbf{B} \cdot d\mathbf{s} \tag{A.1}$$

where Σ is any surface with edge $\mathcal{C}$. Since the rectangular loop lies in the plane, we can define the surface of integration to be the same rectangle as the shape of the loop. Furthermore, $\mathbf{B}$ and ds are parallel, so we can just take the magnitude of the magnetic

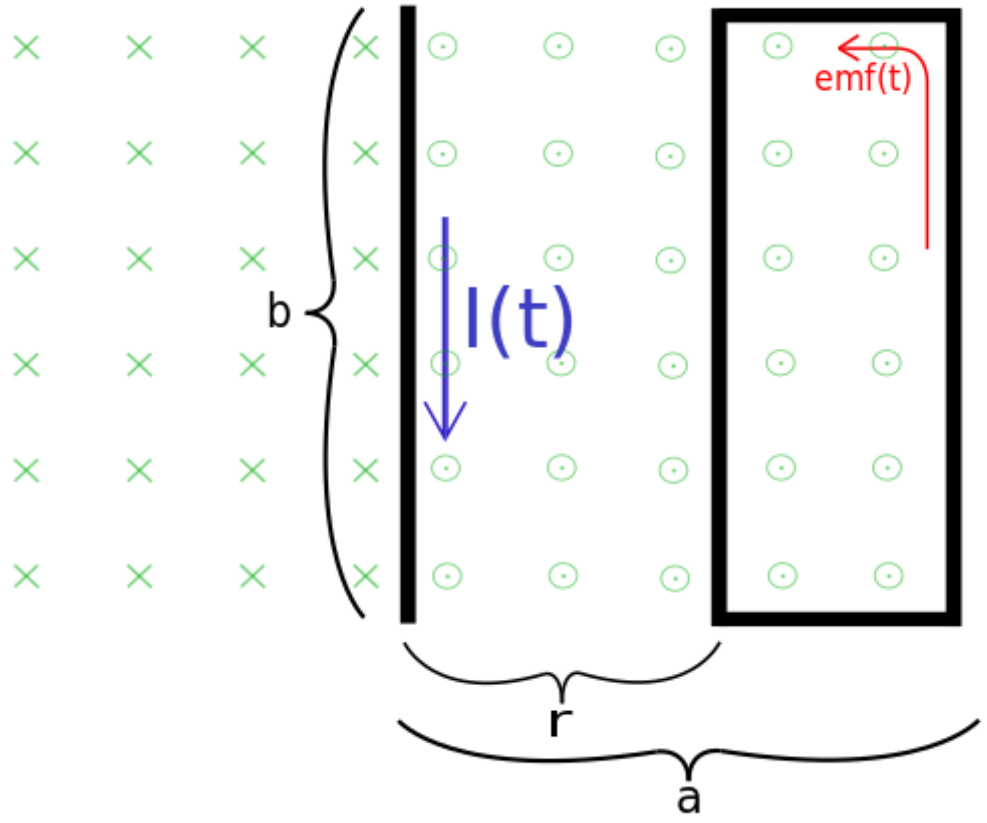

FIGURE A.1: Schematic of validation model.

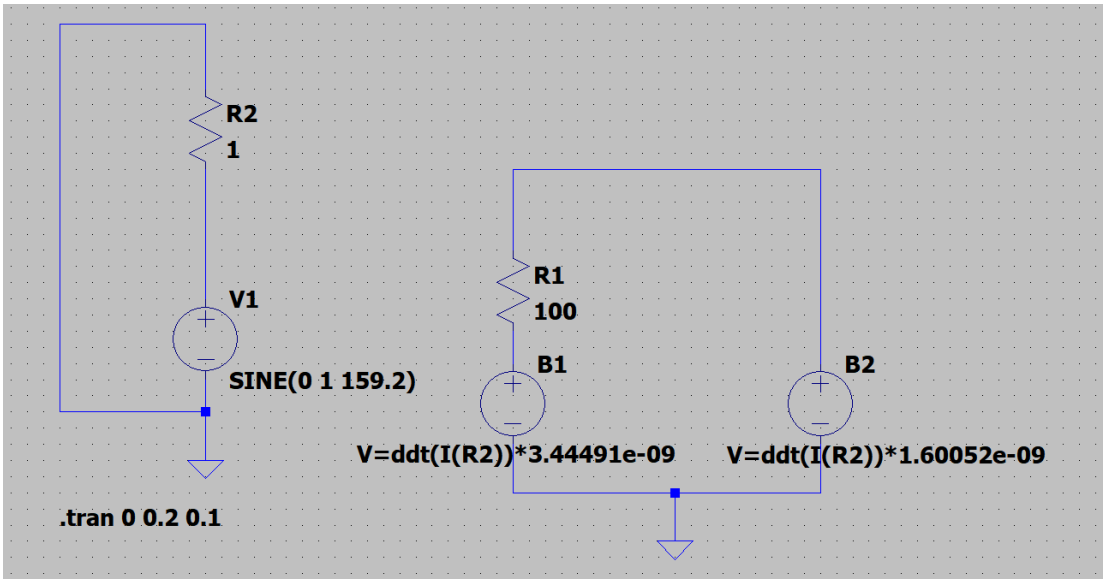

FIGURE A.2: LTPSICE schematic of validation model.

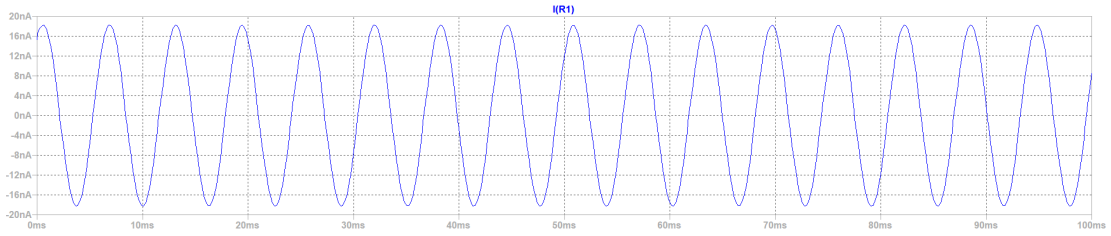

FIGURE A.3: Current resulting from simulated validation model.

field B.

$$\varepsilon = -\frac{\partial}{\partial t}\int_r^a \int_0^b B(x,y)dxdy \tag{A.2}$$

We need to determine the magnetic field as a function of x and y. We use another analytical tool, the Biot-Savart law [11]

$$\mathbf{B}(t) = \frac{\mu_0 I(t)}{4\pi}\oint_{\mathcal{C}} \frac{d\mathbf{l}\times\hat{r}}{\mathbf{r}^2} \tag{A.3}$$

which leads to the integral

$$\varepsilon = -\frac{\partial I(t)}{\partial t}\frac{\mu_0}{4\pi}\int_0^b \int_r^a \int_0^b \frac{y}{\sqrt{(l-x)^2+y^2}^3}dxdydl \tag{A.4}$$

where l is a coordinate that runs the length of the wire. Evaluating this integral yields an induced voltage of 2.04 μV. This shows good agreement with the simulation and validates the model. We note that we use a numerical integration program to evaluate the integral.

Bibliography

[1] Ron W. Darbeau. Nuclear magnetic resonance (NMR) spectroscopy: A review and a look at its use as a probative tool in deamination chemistry. *Applied Spectroscopy Reviews*, 41(4):401–425, August 2006. doi: 10.1080/05704920600726175. URL https://doi.org/10.1080/05704920600726175.

[2] Emmanuel Hatzakis. Nuclear magnetic resonance (NMR) spectroscopy in food science: A comprehensive review. *Comprehensive Reviews in Food Science and Food Safety*, 18(1):189–220, November 2018. doi: 10.1111/1541-4337.12408. URL https://doi.org/10.1111/1541-4337.12408.

[3] Armin Ettl, Christa Fischer-Klein, Andreas Chemelli, Albert Daxer, and Stephan Felber. Nuclear magnetic resonance spectroscopy. *International Ophthalmology*, 18(3):171–181, 1994. doi: 10.1007/bf00915968. URL https://doi.org/10.1007/bf00915968.

[4] Joseph P Hornak. *The Basics of NMR*. URL https://www.cis.rit.edu/htbooks/nmr/inside.htm.

[5] Daniel V Schroeder. *An Introduction to Thermal Physics*. Addison-Wesley, Boston, MA, 2000.

[6] F. Bloch. Nuclear induction. *Physical Review*, 70(7-8):460–474, October 1946. doi: 10.1103/physrev.70.460. URL https://doi.org/10.1103/physrev.70.460.

[7] Jaan Kiusalaas. *Numerical Methods in Engineering with Python 3*. Cambridge University Press, USA, 3rd edition, 2013. ISBN 1107033853.

[8] P.T. Callaghan, C.D. Eccles, T.G. Haskell, P.J. Langhorne, and J.D. Seymour. Earth's field NMR in antarctica: A pulsed gradient spin echo NMR study of restricted diffusion in sea ice. *Journal of Magnetic Resonance*, 133(1):148–154, July 1998. doi: 10.1006/jmre.1998.1417. URL https://doi.org/10.1006/jmre.1998.1417.

[9] J. Stepišnik, V. Eržen, and M. Kos. NMR imaging in the earth's magnetic field. *Magnetic Resonance in Medicine*, 15(3):386–391, September 1990. doi: 10.1002/mrm.1910150305. URL https://doi.org/10.1002/mrm.1910150305.

[10] Carl A Michal. A low-cost spectrometer for NMR measurements in the earth's magnetic field. *Measurement Science and Technology*, 21(10):105902, August 2010. doi: 10.1088/0957-0233/21/10/105902. URL https://doi.org/10.1088/0957-0233/21/10/105902.

[11] David J Griffiths. *Introduction to electrodynamics; 3rd ed.* Prentice-Hall, Upper Saddle River, NJ, 1999.

[12] C. L. W. Sonntag, E. A. Lomonova, and J. L. Duarte. Implementation of the neumann formula for calculating the mutual inductance between planar PCB inductors. In *2008 18th International Conference on Electrical Machines*. IEEE, September 2008. doi: 10.1109/icelmach.2008.4799978. URL https://doi.org/10.1109/icelmach.2008.4799978.